



ORIGINAL ARTICLE

Bayesian regularization networks for micropolar ternary hybrid nanofluid flow of blood with homogeneous and heterogeneous reactions: Entropy generation optimization



Bhupendra K. Sharma^a, Parikshit Sharma^a, Nidhish K. Mishra^b,
 Samad Noeiaghdam^{c,d,*}, Unai Fernandez-Gamiz^e

^a Department of Mathematics, Birla Institute of Technology and Science, Pilani, India

^b Department of Basic Sciences, College of Sciences and Theoretical Studies, Saudi Electronic University, Riyadh 11673, Saudi Arabia

^c Industrial Mathematics Laboratory, Baikal School of BRICS, Irkutsk National Research Technical University, Irkutsk 664074, Russia

^d Department of Applied Mathematics and Programming, South Ural State University, Lenin Prospect 76, Chelyabinsk 454080, Russia

^e Nuclear Engineering and Fluid Mechanics Department, University of the Basque Country UPV/EHU, Nieves Cano 12, 01006 Vitoria-Gasteiz, Spain

Received 17 March 2023; revised 1 June 2023; accepted 21 June 2023

Available online 3 July 2023

KEYWORDS

Ternary hybrid nanofluid;
 Curved artery;
 Bayesian regularization
 backpropagation algorithm;
 Homogeneous and hetero-
 geneous chemical reactions

Abstract This study aims to analyze a Bayesian regularization backpropagation algorithm for micropolar ternary hybrid nanofluid flow over curved surfaces with homogeneous and heterogeneous reactions, Joule heating and viscous dissipation. The ternary hybrid nanofluid consists of nanoparticles of titanium oxide (TiO₂), copper oxide (CuO), and silicon oxide (SiO₂), with blood as the base fluid. The governing partial differential equations for the fluid flow are converted into ordinary differential equations using a group of self-similar transformations. The ordinary differential equations are solved using an appropriate shooting algorithm in MATLAB. The effects of physical parameters including curvature, micro-polar, radiation, magnetic, Prandtl, Eckert, Schmidt, and homogeneous and heterogeneous chemical reaction parameters are analyzed for velocity, micro rotational, temperature, and concentration profile. Physical quantities of engineering interest like heat transfer rate, mass transfer rate, skin friction coefficient, couple stress coefficient, and entropy generation are also discussed in this study. A Bayesian regularization backpropagation algorithm is also designed for the solution of the ordinary differential equations. The obtained network is ana-

* Corresponding author at: Industrial Mathematics Laboratory, Baikal School of BRICS, Irkutsk National Research Technical University, Irkutsk 664074, Russia.

E-mail addresses: bhupen_1402@yahoo.co.in (B.K. Sharma), parikshitsharma2001@gmail.com (P. Sharma), n.kumar@seu.edu.sa (N.K. Mishra), snoei@istu.edu (S. Noeiaghdam), unai.fernandez@ehu.eus (U. Fernandez-Gamiz).

Peer review under responsibility of Faculty of Engineering, Alexandria University.

<https://doi.org/10.1016/j.aej.2023.06.080>

1110-0168 © 2023 The Authors. Published by Elsevier BV on behalf of Faculty of Engineering, Alexandria University.

This is an open access article under the CC BY-NC-ND license (<http://creativecommons.org/licenses/by-nc-nd/4.0/>).

Nomenclature

Subscripts

f	Fluid
nf	Nanofluid
hnf	Hybrid nanofluid
thnf	Ternary hybrid nanofluid

Symbols

(r, s)	Curvilinear coordinates
R	Radius of curved surface
U	Velocity component in the s direction
V	Velocity component in the r direction
N	Micro-rotation velocity
V_0	Mass-flux velocity
T_w	Sheet temperature
T_∞	Ambient temperature
T	Dimensionless temperature
B_0	Uniform magnetic field
η	Similarity variable
O	Origin
U_w	Stretching velocity
a	Initial stretching rate ($a > 0$)
λ	Shrinking ($\lambda < 0$) or stretching ($\lambda > 0$) constant
n	Turbulent flow constant
P	Pressure

$p(\eta)$	Dimensionless Pressure
ν	Kinematic viscosity
μ	Dynamic viscosity
k	Thermal conductivity
ρ	Density
c_p	Specific heat
$f(\eta)$	Dimensionless velocity component in the r direction
$g(\eta)$	Dimensionless velocity component in the s direction
ϕ_{CuO}	Concentration of CuO
ϕ_{TiO_2}	Concentration of TiO_2
ϕ_{SiO_2}	Concentration of SiO_2
$\theta(\eta)$	Dimensionless temperature
$\phi(\eta)$	Dimensionless concentration
$h(\eta)$	Dimensionless concentration
k^*	Vortex viscosity
σ^*	Stefan - Boltzmann constant
k_{Rd}	Absorption coefficient
k_r	Homogeneous reaction rate constant
k_e	Heterogeneous reaction rate constant
(b, c)	Chemical concentrations
(b_0, c_0)	Initial chemical concentrations
(D_B, D_C)	Diffusion coefficients

lyzed using training state, performance, error histograms, model response, Error autocorrelation, and input-error correlation plots. It is observed that the entropy generation and the Bejan number increase for enhancing Brinkman and radiation parameter. Clinical researchers and biologists may use the results of this computational study to forecast endothelial cell damage and plaque deposition in curved arteries, by which the severity of these conditions can be reduced.

© 2023 The Authors. Published by Elsevier BV on behalf of Faculty of Engineering, Alexandria University. This is an open access article under the CC BY-NC-ND license (<http://creativecommons.org/licenses/by-nc-nd/4.0/>).

1. Introduction

The nanoparticles fluid suspensions are newly discovered nanotechnology-based heat transfer fluids with enhanced thermal properties. These properties are superior to the properties of the base fluids that host the nanoparticles and the conventional particle fluid suspensions. Nanofluids are produced by dispersing and then stably suspending nanoparticles with typical dimensions of 10 nm. Rafiq et al. [1] studied the peristaltic mechanism of nanomaterial with couple stress in a tapered channel and provided insights into the behaviour of nanofluids in peristaltic motion. Yadav et al. [2] presented an analytic solution of a dual-porosity fractional model to simulate groundwater flow in a karstic aquifer and predicted groundwater movement in karstic systems. Blood offers potential for advancements in diagnostics, therapeutics, and medical treatments. Gul et al. [3] investigated the mixed convection stagnation point flow of a blood-based hybrid nanofluid around a rotating sphere. Saeed et al. [4] explored the flow of a blood-

based hybrid nanofluid in the presence of an electromagnetic field and couple stresses. Alnahdi et al. [5] focused on the application of a blood-based ternary hybrid nanofluid flowing through a perforated capillary, specifically for drug delivery purposes. They examined the behaviour and performance of the nanofluid in this context, providing insights that could potentially contribute to advancements in drug delivery systems. Shrinking stretching surface in nanofluids induce a flow that enhances heat transfer and fluid mixing due to the dynamic changes in the boundary layer thickness, resulting in improved convective heat transfer and enhanced nanoparticle dispersion. Saeed et al. [6] conducted a theoretical analysis of unsteady squeezing nanofluid flow, considering the physical properties of the fluid. Khan et al. [7,8] studied the electro viscous effect of water-based nanofluid flow between two parallel disks with suction/injection effect is investigated. Javed et al. [9] studied the axisymmetric flow of a Casson fluid induced by a swirling cylinder. Dadheech et al. [10,11,12] investigated the Marangoni convection flow of $\gamma\text{-Al}_2\text{O}_3$ nanofluids past a

porous stretching surface in the presence of thermal radiation and an inclined magnetic field. Their findings highlighted the impact of these factors on the heat transfer rate, velocity profiles, and temperature distribution in the nanofluid flow.

External magnetic field used in nanofluids alters the flow behaviour, heat transfer characteristics, and particle distribution within the nanofluid. Dinarvand et al. [13] studied the squeezing flow of aqueous CNTs-Fe₃O₄ hybrid nanofluid and analysed the effects of heat source/sink, nanoparticle shape, and an oblique magnetic field and investigated these factors on the flow behaviour and performance. Khan et al. [14] conducted a numerical analysis of unsteady hybrid nanofluid flow consisting of CNTs-ferrous oxide/water with a variable magnetic field. They studied magnetic field characteristics on the flow. Rafiq et al. [15] theoretically explored thermal transportation with Lorentz force for a fourth-grade fluid model under peristaltic mechanism. Their main result involved investigating the effects of the Lorentz force. Rehman et al. [16] investigated the MHD flow of carbon in micropolar nanofluid with convective heat transfer in the rotating frame. Their main result focused on analysing the influence of the rotating frame and magnetic field on the flow behaviour. Kumar et al. [17] performed response surface optimization for the electromagnetohydrodynamic Cu-polyvinyl alcohol/water Jeffrey nanofluid flow with an exponential heat source. Thermal radiations play a crucial role in nanofluid heat transfer processes, influencing thermal conductivity, convective heat transfer, and energy absorption characteristics. Dharmiah et al. [18] developed a non-homogeneous two-component Buongiorno model to investigate the nanofluid flow towards Howarth's wavy cylinder with activation energy. Dharmiah et al. [19] studied the Arrhenius activation energy of a tangent hyperbolic nanofluid flowing over a cone with radiation absorption. The authors studied thermal radiation behaviour of the nanofluid. Abbas et al. [20] examined the oscillatory slip flow of Fe₃O₄ and Al₂O₃ nanoparticles in a vertical porous channel using Darcy's law and thermal radiation. Abbas et al. [21] investigated the peristaltic transport of a Casson fluid in a non-uniform inclined tube considering the Rosseland approximation and wall properties. The study demonstrated thermal effects on the flow characteristics and temperature distribution.

Heat transfer rate in nanofluids plays an important role in enhancing thermal conductivity and overall heat transfer efficiency due to the presence of nanoparticles. Shah et al. [22] conducted a computational analysis on radiative engine oil-based Prandtl-Eyring hybrid nanofluid flow with variable heat transfer using the Cattaneo-Christov heat flux model. Tang et al. [23] performed a computational study on magnetized gold-blood Oldroyd-B nanofluid flow and heat transfer in stenosis narrow arteries. Abbas et al. [24] investigated the thermally developed generalized Bödewadt flow containing nanoparticles over a rotating surface with slip condition. Their study focused on the flow behaviour and heat transfer characteristics of the nanofluid, considering the presence of slip condition at the surface. They provided insights into the thermal development and flow patterns of the nanofluid over a rotating surface. Mass transfer rate helps in determining the dispersion and distribution of nanoparticles within the fluid, affecting their stability and overall performance in various applications. Alnahdi et al. [25] investigated the flow of couple stress ternary hybrid nanofluid in a contraction channel for drug delivery

purposes. Gandhi et al. [26] conducted a study on entropy generation and shape effects in the context of hybrid nanoparticles (Cu-Al₂O₃/blood)-mediated blood flow through a time-variant multi-stenotic artery. Their research aimed to understand the influence of nanoparticle shape and other factors on mass transfer rate.

Viscous dissipation refers to the conversion of mechanical energy into heat due to the internal friction within a fluid. In the human body, viscous dissipation plays a role in increasing the overall temperature of blood and tissues during blood flow. Hameed et al. [27] presented an analytical analysis of the magnetic field, heat generation and absorption, and viscous dissipation effects on couple stress Casson hybrid nanofluid flow over a nonlinear stretching surface. Rafiq and Abbas [28] investigated the impacts of viscous dissipation and thermal radiation on a Rabinowitsch fluid model that follows a peristaltic mechanism with wall properties. Khanduri and Sharma [29] focused on the mathematical analysis of the Hall effect and hematocrit-dependent viscosity in Au/GO-Blood hybrid nanofluid flow through a stenosed catheterized artery with thrombosis. The main outcome emphasizes the influence of these factors on the flow behaviour and the formation of thrombosis in stenosed arteries. Gandhi and Sharma [30] presented a mathematical model for pulsatile blood flow using the Casson fluid model through an overlapping stenotic artery with Au-Cu hybrid nanoparticles. The main result highlights the impact of varying viscosity on the flow characteristics and the distribution of nanoparticles in the artery. Brownian motion governs the random movement of particles, such as molecules and nanoparticles, within biological systems. Tawade et al. [31] studied the effects of thermophoresis and Brownian motion on thermal and chemically reacting Casson nanofluid flow over a linearly stretching sheet. Gupta et al. [32] conducted a numerical study of the flow of two radiative nanofluids with Marangoni convection embedded in a porous medium.

Entropy generation provides a quantitative measure of the system's energy dissipation and aids in optimizing nanofluid applications by minimizing entropy generation and maximizing thermal performance. Nisar et al. [33] investigated the entropy generation and activation energy in nonlinear mixed convection flow of a tangent hyperbolic nanofluid. Khan et al. [34] focused on entropy generation optimization in mixed convection nanomaterial flow. The study highlighted important aspects related to the efficiency and irreversibility of the flow process, providing valuable information for optimizing nanofluid flow systems. Sharma et al. [35] conducted an optimization study on heat transfer in nanofluid blood flow through a stenosed artery, considering the presence of the Hall effect and hematocrit-dependent viscosity. These studies optimized entropy generation and provided insights into the thermodynamic behaviour of the nanofluid flow. Homogeneous reactions occur within the same phase, such as enzyme-catalysed reactions, while heterogeneous reactions take place at the interface between different phases, such as the absorption and digestion of nutrients in the gastrointestinal tract. Arulmozhi et al. [36] investigated the heat and mass transfer characteristics of a magnetohydrodynamic (MHD) nanofluid flowing over an infinite moving vertical plate. Khan et al. [37] studied the chemically reactive flow of an upper-convected Maxwell fluid using the Cattaneo-Christov heat flux model.

The involvement of machine learning, deep learning, and computer vision is increasing in our lives. Like the known and famous ANNs, this study uses the Bayesian regularization backpropagation algorithm to investigate this ternary hybrid nanofluid problem. The algorithm is used in MATLAB using a time series and neural network toolbox. The need for extensive cross-validation can be decreased or eliminated with Bayesian regularization back propagation (BRBP) algorithm, which are more resilient than traditional backpropagation algorithms. A mathematical technique known as Bayesian regularization turns a nonlinear regression into a well-posed statistical problem like ridge regression. The benefit of BRBP is that the models are robust, eliminating the need for the validation procedure, which scales as $O(N^2)$ in conventional regression techniques like backpropagation. These networks offer solutions to issues that emerge in Quantitative structure–activity relationship (QSAR) modelling, including model selection, robustness, validation set selection, validation effort size, and network architectural optimization. As evidence processes offer an impartial Bayesian criterion for ceasing training, it isn't easy to overtrain them. Because the BRBP calculates and trains on many effective network characteristics or weights, essentially turning off insignificant ones, they are also challenging to overfit. Typically, this effective value is much lower than the weights in a typical fully linked backpropagation neural network. Ali et al. [38] used an intelligent computing approach with a Levenberg-Marquardt artificial neural network to study the behaviour of carbon nanotubes dispersed in water between stretchable rotating disks. Khan et al. [39] designed backpropagated intelligent networks for nonlinear second-order Lane-Emden pantograph delay differential systems. Khan et al. [40] proposed the design of a neural network using Levenberg-Marquardt and Bayesian regularization backpropagation techniques to solve pantograph delay differential equations. Their main result was the development of an efficient computational model capable of accurately solving these equations, which can have applications in various fields such as physics and engineering. From the above literature review, it can be concluded that the following are the novelty of the present study:

- Ternary hybrid nanofluid consisting of nanoparticles of titanium oxide (TiO_2), copper oxide (CuO), and silicon oxide (SiO_2) is investigated with blood as the base fluid.
- The combined effect of thermal radiation, magnetic field, homogeneous and heterogeneous chemical reactions, Joule heating, and viscous dissipation on blood flow through curved artery is examined.
- Bayesian regularization backpropagation algorithm for the ternary hybrid nanofluid's training state, performance, error histograms, model response, error autocorrelation, and input-error correlation plots are analyzed.

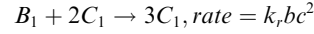
2. Problem formulation

Considered a micropolar, incompressible, pseudoplastic, and electrically conducting $\text{CuO-TiO}_2\text{-SiO}_2/\text{Blood}$ ternary hybrid nanofluid flows through a curved surface of radius of curvature, R . Curvilinear coordinate systems (r, s) is considered to formulate the physical model. A uniform external magnetic

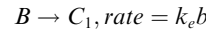
field of strength B_0 is applied perpendicular to the surface. Thermal radiation, viscous dissipation, and joule heating with homogenous and heterogeneous chemical reactions govern the mass transfer phenomena of the ternary hybrid nanofluid are also considered. The curved surface can stretch or shrink (opposite of stretch) as shown in Figs. 1a and 1b. The physical model is shown in Fig. 1c.

The stretching of surface happens in the positive s - direction and shrinking happens in the negative s - direction with velocity, $U_w = as$, where a is a positive constant representing the initial stretching rate. V_0 is the mass-flux velocity, $V_0 < 0$ represents injection, and $V_0 > 0$ represents suction. Physical model of the problem is depicted in Fig. 1c.

The homogeneous chemical reaction is defined as: [41]



and the heterogeneous chemical reaction is defined as:



where k_r and k_c are the rate constants. b is the concentration of species B_1 , and c is the concentration of species C_1 . The governing equations of the fluid flow problem with above assumptions can be written as [41–45]:

$$\frac{\partial}{\partial r} [V(r+R)] + R \frac{\partial U}{\partial s} = 0, \quad (1)$$

$$\frac{U^2}{r+R} = \frac{1}{\rho_{thnf}} \frac{\partial P}{\partial r}, \quad (2)$$

$$\begin{aligned} V \frac{\partial U}{\partial r} + \frac{R}{r+R} U \frac{\partial U}{\partial s} = & -\frac{1}{\rho_{thnf}} \frac{R}{r+R} \frac{\partial P}{\partial s} - \frac{UV}{r+R} - \frac{k^*}{\rho_{thnf}} \frac{\partial N}{\partial r} \\ & + \frac{(\mu_{thnf} + k^*)}{\rho_{thnf}} \left[\frac{\partial^2 U}{\partial r^2} + \frac{1}{r+r} \frac{\partial U}{\partial r} - \frac{U}{(r+R)^2} \right] \\ & - \frac{\sigma_{thnf}}{\rho_{thnf}} B_0^2 U, \end{aligned} \quad (3)$$

$$\begin{aligned} V \frac{\partial N}{\partial r} + \frac{R}{r+R} U \frac{\partial N}{\partial s} = & \frac{\gamma}{\rho_{thnf} \beta^*} \left(\frac{1}{r+R} \frac{\partial N}{\partial r} + \frac{\partial U}{\partial s} \right) \\ & - \frac{k^*}{\rho_{thnf} \beta^*} \left(2N + \frac{U}{r+R} + \frac{\partial U}{\partial r} \right), \end{aligned} \quad (4)$$

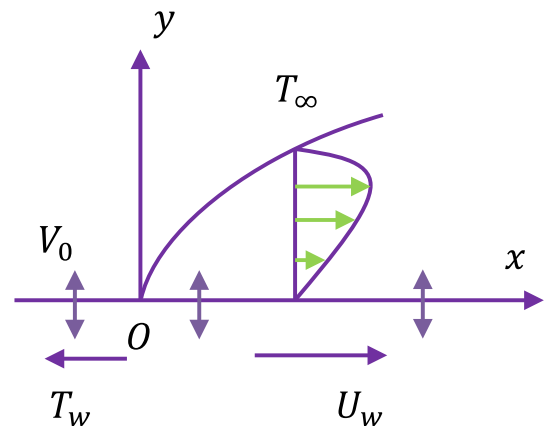


Fig. 1a Curved surface stretching.

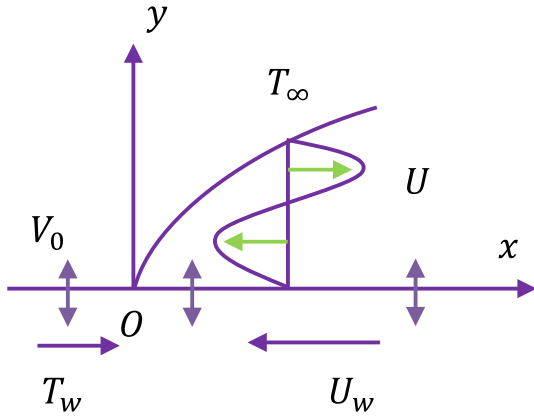


Fig. 1b Curved surface shrinking.

$$\begin{aligned}
 V \frac{\partial T}{\partial r} + \frac{R}{r+R} U \frac{\partial T}{\partial s} &= \frac{k_{thnf}}{(\rho C_p)_{thnf}} \left[\frac{1}{r+R} \frac{\partial T}{\partial r} + \frac{\partial^2 T}{\partial r^2} \right] \\
 &\quad - \frac{1}{(\rho C_p)_{thnf}} \frac{1}{r+R} \frac{\partial}{\partial r} [q_r(r+R)] \\
 &\quad + \frac{(\mu_{thnf} + k^*)}{(\rho C_p)_{thnf}} \left(\frac{\partial U}{\partial r} - \frac{U}{r+R} \right)^2 \\
 &\quad + \frac{\sigma_{thnf}}{(\rho C_p)_{thnf}} B_0^2 U^2, \tag{5}
 \end{aligned}$$

$$D_B \left(\frac{\partial^2 b}{\partial r^2} + \frac{1}{r+R} \frac{\partial b}{\partial r} \right) - k_r b c^2 = V \frac{\partial b}{\partial r} + \frac{R}{r+R} U \frac{\partial b}{\partial s}, \tag{6}$$

$$D_C \left(\frac{\partial^2 c}{\partial r^2} + \frac{1}{r+R} \frac{\partial c}{\partial r} \right) - k_r b c^2 = V \frac{\partial c}{\partial r} + \frac{R}{r+R} U \frac{\partial c}{\partial s} \tag{7}$$

Where, q_r is the radiation heat flux, and mathematically expressed in accordance with the Rosseland estimation as:

$$q_r = -\frac{4}{3} \frac{\sigma^*}{k_{Rd}} \frac{\partial T^4}{\partial r}$$

Where, k_{Rd} is the absorption coefficient, and σ^* is the Stefan-Boltzmann constant. By assuming that the temperature diffusion inside the flow is sufficiently modest, the term T^4 may well as a linear temperature function in the Taylor series with respect to T_∞ and ignoring the higher expressions, leading to:

$$T^4 \approx -3T_\infty^4 + 4TT_\infty^3$$

Hence, Eq. (5) can be expressed as:

$$\begin{aligned}
 V \frac{\partial T}{\partial r} + \frac{R}{r+R} U \frac{\partial T}{\partial s} &= \frac{k_f}{(\rho C_p)_{thnf}} \left[\frac{1}{r+R} \frac{\partial T}{\partial r} + \frac{\partial^2 T}{\partial r^2} \right] \left(\frac{k_{thnf}}{k_f} + \frac{4}{3} Rd \right) \\
 &\quad + \frac{(\mu_{thnf} + k^*)}{(\rho C_p)_{thnf}} \left(\frac{\partial U}{\partial r} - \frac{U}{r+R} \right)^2 + \frac{\sigma_{thnf}}{(\rho C_p)_{thnf}} B_0^2 U^2 \tag{8}
 \end{aligned}$$

The boundary conditions of the considered model are:

$$\left. \begin{aligned}
 U &= a\lambda s, V = V_0, N = -n \frac{\partial U}{\partial r}, T = T_w, D_B \frac{\partial b}{\partial r} \\
 &= k_r b, D_C \frac{\partial c}{\partial r} = -k_r b, a r = 0 \\
 U &\rightarrow 0, \frac{\partial U}{\partial r} \rightarrow 0, N \rightarrow 0, T \rightarrow T_\infty, a \rightarrow a_0, b \rightarrow 0, a s r \rightarrow \infty
 \end{aligned} \right\} \tag{9}$$

Where, k_{thnf} , ν_{thnf} , σ_{thnf} , and μ_{thnf} are thermal conductivity, kinematic viscosity, electrical conductivity, and dynamic viscosity of the hybrid nanofluid, respectively. For the considered hybrid nanofluid, the thermophysical properties are presented in Table 1 and mathematically expressed as [46]: The different cases and values of the physical parameters are shown in Table 2. Table 3 contains the reference and default values of flow parameters.

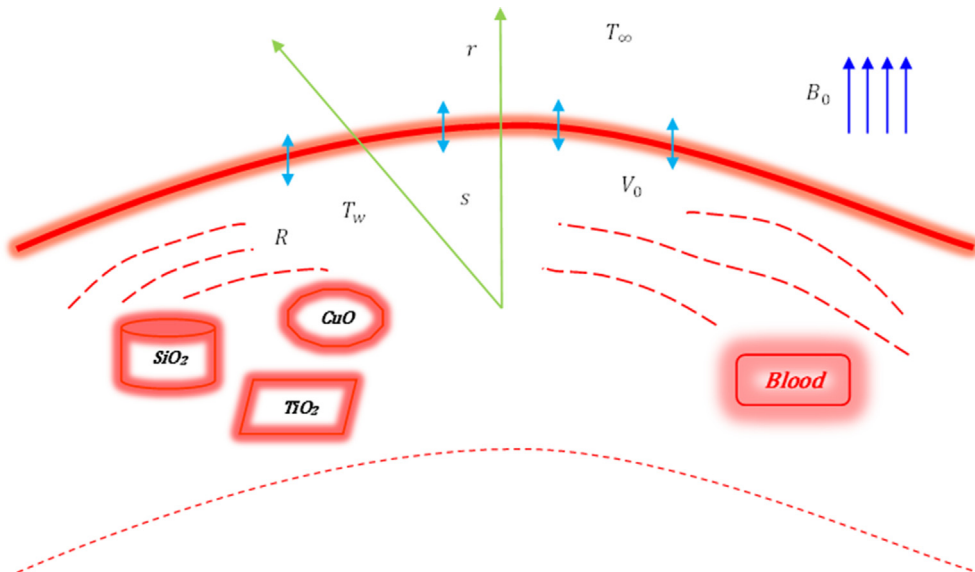


Fig. 1c Physical model of the problem.

$$\begin{aligned} \frac{\mu_{hnf}}{\mu_f} &= [(1 - \phi_{CuO})(1 - \phi_{TiO_2})(1 - \phi_{SiO_2})]^{-2.5}, \\ \frac{\rho_{hnf}}{\rho_f} &= (1 - \phi_{CuO}) \left[(1 - \phi_{TiO_2}) \left\{ (1 - \phi_{SiO_2}) + \phi_{SiO_2} \frac{\rho_{SiO_2}}{\rho_f} \right\} + \phi_{TiO_2} \frac{\rho_{TiO_2}}{\rho_f} \right] + \phi_{CuO} \frac{\rho_{CuO}}{\rho_f}, \\ \frac{(\rho C_p)_{hnf}}{(\rho C_p)_f} &= (1 - \phi_{CuO}) \left[(1 - \phi_{TiO_2}) \left\{ (1 - \phi_{SiO_2}) + \phi_{SiO_2} \frac{(\rho C_p)_{SiO_2}}{(\rho C_p)_f} \right\} + \phi_{TiO_2} \frac{(\rho C_p)_{TiO_2}}{(\rho C_p)_f} \right] + \phi_{CuO} \frac{(\rho C_p)_{CuO}}{(\rho C_p)_f}, \\ \frac{\sigma_{hnf}}{\sigma_f} &= \left[\frac{\sigma_{SiO_2} + 2\sigma_f - 2\phi_{SiO_2}(\sigma_f - \sigma_{SiO_2})}{\sigma_{SiO_2} + 2\sigma_f + \phi_{SiO_2}(\sigma_f - \sigma_{SiO_2})} \right], \\ \frac{\sigma_{hnf}}{\sigma_f} &= \left[\frac{\sigma_{TiO_2} + 2\sigma_f - 2\phi_{TiO_2}(\sigma_f - \sigma_{TiO_2})}{\sigma_{TiO_2} + 2\sigma_f + \phi_{TiO_2}(\sigma_f - \sigma_{TiO_2})} \right], \\ \frac{\sigma_f}{\sigma_f} &= \left[\frac{\sigma_{CuO} + 2\sigma_f - 2\phi_{CuO}(\sigma_f - \sigma_{CuO})}{\sigma_{CuO} + 2\sigma_f + \phi_{CuO}(\sigma_f - \sigma_{CuO})} \right], \\ \frac{k_{hnf}}{k_f} &= \left[\frac{k_{SiO_2} + 2k_f - 2\phi_{SiO_2}(k_f - k_{SiO_2})}{k_{SiO_2} + 2k_f + \phi_{SiO_2}(k_f - k_{SiO_2})} \right], \\ \frac{k_{hnf}}{k_f} &= \left[\frac{k_{TiO_2} + 2k_f - 2\phi_{TiO_2}(k_f - k_{TiO_2})}{k_{TiO_2} + 2k_f + \phi_{TiO_2}(k_f - k_{TiO_2})} \right], \\ \frac{k_f}{k_f} &= \left[\frac{k_{CuO} + 2k_f - 2\phi_{CuO}(k_f - k_{CuO})}{k_{CuO} + 2k_f + \phi_{CuO}(k_f - k_{CuO})} \right], \\ \phi &= \phi_{SiO_2} + \phi_{TiO_2} + \phi_{CuO} \end{aligned} \tag{10}$$

Now, a group of self-similar transformation will be used to convert the above partial differential equations (PDEs) into ordinary differential equations (ODEs). The self-similar transformation involves introducing dimensionless variable that captures the scaling behavior of the nanofluid flow. These transformations help in simplifying the governing equations by reducing the number of independent variables. The transformed PDEs will be expressed in terms of ODEs having a single independent variable. The obtained ODEs will be then numerically solved using BVP5C shooting method in MATLAB. This simplification allows for a more tractable analysis and a better understanding of the underlying physical phenomena in nanofluids.

The following transformations are used to convert the system of partial differential equations (1) to (7) into ordinary differential equations:

$$\begin{aligned} V &= -\sqrt{av_f} \frac{R}{r+R} f, U = asf', \theta = \frac{T - T_\infty}{T_w - T_\infty}, \\ P &= \rho_f a^2 s^2 p, N = as \sqrt{\frac{a}{\nu_f}} g, b = b_0 \phi, c = c_0 h, \eta = r \sqrt{\frac{a}{\nu_f}} \end{aligned} \tag{11}$$

Equations (2)–(6) reduce into the following ordinary differential equations:

$$p' = A_1 \frac{1}{\eta + \beta} (f')^2, \tag{12}$$

$$\begin{aligned} \frac{2}{A_1} \frac{\beta}{\eta + \beta} p &= \frac{\beta}{\eta + \beta} [ff'' - (f')^2] + \frac{\beta}{(\eta + \beta)^2} ff' - \frac{K_1}{A_1} g' \\ &+ \left(\frac{A_2}{A_1} + \frac{K_1}{A_1} \right) \left[f''' + \frac{1}{\eta + \beta} f'' - \frac{1}{(\eta + \beta)^2} f' \right] \\ &- Mf', \end{aligned} \tag{13}$$

Table-2 Values used for curve plotting.

Parameter	Case-1	Case-2	Case-3
β	2.0	2.2	2.4
M	1.8	1.9	2.0
Rd	7.0	8.0	9.0
Pr	21	22	23
K_1	0.05	0.10	0.15
Kr_1	0.10	0.15	0.20
Kr_2	0.01	0.05	0.10
ϕ_{CuO}	0.005	0.020	0.035
ϕ_{TiO_2}	0.005	0.020	0.035
ϕ_{SiO_2}	0.005	0.020	0.035

$$\begin{aligned} &\left(\frac{A_2}{A_1} + \frac{K_1}{2A_1} \right) \left[g'' + \frac{1}{\eta + \beta} g' \right] + \frac{\beta}{\eta + \beta} [fg' - gf'] \\ &- \frac{K_1}{A_1} \left[f'' + \frac{1}{\eta + \beta} f' + 2g \right] \\ &= 0 \end{aligned} \tag{14}$$

$$\begin{aligned} A_4 \frac{\beta}{\eta + \beta} Pr f \theta' &+ \left(A_3 + \frac{4}{3} Rd \right) \left[\frac{1}{\eta + \beta} \theta' + \theta'' \right] + \frac{1}{A_4} M Br \\ &+ \frac{1}{A_5} Br (A_2 + K_1) \left(f'' - \frac{f'}{\eta + \beta} \right)^2 \\ &= 0 \end{aligned} \tag{15}$$

$$\frac{1}{Sc} \left(\phi'' + \frac{1}{\eta + \beta} \phi' \right) - Kr_1 \phi (1 - \phi)^2 + \frac{\beta}{\eta + \beta} f \phi' = 0 \tag{16}$$

Where the dimensionless parameters are defined as follows:

Radius of curvature (ROC) parameter: $\beta = R \sqrt{\frac{a}{\nu_f}}$, Micro polar parameter: $K_1 = \frac{k^*}{\mu_f}$,

Micro inertia parameter: $j^* = \frac{\mu_f}{\rho_f a^2}$, Spin gradient parameter: $\gamma = \frac{2\mu_{thnf} + k^*}{2}$,

Radiation parameter: $Rd = \frac{4\sigma^* T_\infty^3}{k_R a^2 k_f}$, Magnetic parameter:

$$M = \frac{B_0^2 \sigma_{thnf}}{a \rho_{thnf}},$$

Prandtl number: $Pr = \frac{\nu_f (\rho C_p)_f}{k_f}$, Eckert number: $Ec = \frac{a^2 s^2}{(T_w - T_\infty) (c_p)_{thnf}}$

Schmidt number: $Sc = \frac{\nu_f}{D_B}$, Homogeneous chemical reaction parameter: $Kr_1 = \frac{k_r c_0^2}{a}$

Heterogeneous chemical reaction parameter: $Kr_2 = \frac{k_c}{D_C} \sqrt{\frac{\nu_f}{a}}$, Brinkman number: $Br = Pr Ec$

Table 1 Thermophysical properties of ternary hybrid nanofluid.

Properties	Notation	Nanoparticles			Base fluid
		CuO	TiO ₂	SiO ₂	Blood
Density (Kg/m3)	ρ	6510	4175	2650	1150
Specific heat (J/kg K)	C_p	540	6012	730	3617
Thermal conductivity (W/m K)	k	18	8.4	1.5	0.53

Table-3 Ranges of the values of physical parameters.

Parameter	β	M	Rd	Br	K_1	Kr_1	Kr_2	ϕ_{CuO}	ϕ_{TiO_2}	ϕ_{SiO_2}
Range	0–5	0–5	0–10	0–6	0–5	0–1	0–1	0–0.1	0–0.1	0–0.1
Reference	[33]	[52]	[53]	[54]	[33]	[41]	[41]	[55]	[55]	[55]

Reynolds number: $Re = \frac{\rho_f U_w}{\mu_f}$, Temperature difference parameter: $H = \frac{\Delta T}{T_\infty} = \frac{T_w - T_\infty}{T_\infty}$

Diffusion parameter: $L_1 = \frac{RD_B b_0}{k_f}$, Bioconvection diffusion parameter: $L_2 = \frac{RD_C c_0}{k_f}$

By removing pressure term from Equation (12) and Equation (13), we get,

$$\begin{aligned}
 & (A_2 + K_1) \left[f^{(4)} + \frac{2f'''}{\eta + \beta} - \frac{f''}{(\eta + \beta)^2} + \frac{f'}{(\eta + \beta)^3} \right] + A_1 \\
 & \times \frac{\beta}{\eta + \beta} (ff''' - f'f'') + A_1 \frac{\beta}{(\eta + \beta)^2} [ff'' - (f')^2] - A_1 \\
 & \times \frac{\beta}{(\eta + \beta)^3} ff' - K_1 \left(g'' + \frac{1}{\eta + \beta} g' \right) \\
 & - A_1 M \left(f'' + \frac{1}{\eta + \beta} f' \right) \\
 & = 0
 \end{aligned} \tag{17}$$

With the corresponding boundary conditions:

$$\left. \begin{aligned}
 f(\eta) = S, f'(\eta) = \lambda, g(\eta) = -n f''(\eta), \theta(\eta) = 1, \phi'(\eta) = Kr_2 \phi(\eta), at\eta = 0 \\
 f'(\eta) \rightarrow 0, f''(\eta) \rightarrow 0, g(\eta) \rightarrow 0, \theta(\eta) \rightarrow 0, \phi(\eta) \rightarrow 1, as\eta \rightarrow \infty
 \end{aligned} \right\} \tag{18}$$

$$\begin{aligned}
 A_1 &= \frac{\rho_{thnf}}{\rho_f}, A_2 = \frac{\mu_{thnf}}{\mu_f}, A_3 = \frac{k_{thnf}}{k_f}, A_4 = \frac{(\rho C_p)_{thnf}}{(\rho C_p)_f}, \\
 A_5 &= \frac{(C_p)_{thnf}}{(C_p)_f}, S = -\frac{V_0}{\sqrt{av_f}}
 \end{aligned}$$

2.1. Engineering quantities of Interests

The physical quantities of interest like heat transfer rate, mass transfer rate, skin friction coefficient, and couple stress coefficient are also analyzed. The Nusselt number, skin friction coefficient, Sherwood number, and couple stress coefficient are mathematically expressed as [47–49]:

$$\begin{aligned}
 Nu &= \frac{s(q_w + q_r)}{k_f(T_w - T_\infty)}, C_f = \frac{\tau_{rs}}{\rho_f U_w^2}, Sh = \frac{s\beta m_w}{R\rho_f D_B b_0}, \\
 C_m &= \frac{v_f M_w}{\rho_f^* U_w^3}
 \end{aligned} \tag{19}$$

Where, $(q_w + q_r)$ is the heat flux, τ_{rs} is the wall friction, m_w is the mass flux, and M_w is the wall couple stress. They are defined as:

$$\begin{aligned}
 q_w &= -k_{thnf} \left(\frac{\partial T}{\partial r} \right)_{r=0}, q_r = -\frac{16}{3} \frac{T_\infty^3 \sigma^*}{k_{Rd}} \left(\frac{\partial T}{\partial r} \right)_{r=0}, \\
 \tau_{rs} &= \left\{ (\mu_{thnf} + k^*) \left[\frac{\partial U}{\partial r} - \frac{U}{r + R} \right] + k^* N \right\}_{r=0}, \\
 m_w &= -\rho_f D_B \left(\frac{\partial b}{\partial r} \right)_{r=0}, M_w = \gamma \left(\frac{\partial N}{\partial r} \right)_{z=0}
 \end{aligned} \tag{20}$$

The non-dimensional form of above expressions are as follows:

$$\begin{aligned}
 NuRe^{-\frac{1}{2}} &= -\left[A_3 + \frac{4}{3} Rd \right] \theta'(0), \\
 C_f Re^{\frac{1}{2}} &= [A_2 + K_1(1 - n)] f''(0) \\
 &- (A_2 + K_1) \frac{f'(0)}{\beta}, ShRe^{-\frac{1}{2}} \\
 &= -\phi'(0), C_m Re = \left(A_2 + \frac{K_1}{2} \right) g'(0)
 \end{aligned} \tag{21}$$

2.2. Entropy generation

The mathematical definition of entropy generation in a process caused by viscous dissipation, Ohmic heating, and convection-radiation-based heat transfer in the problem using second law of thermodynamics is as follows [50–51]:

$$\begin{aligned}
 S_{gen} &= \frac{k_{thnf}}{T_\infty^2} \left(\frac{\partial T}{\partial r} \right)^2 + \frac{k_{thnf}}{T_\infty^2} \frac{16}{3} \frac{\sigma^* T_\infty^3}{k_f k_{Rd}} \left(\frac{\partial T}{\partial r} \right)^2 \\
 &+ \frac{(\mu_{thnf} + k^*)}{T_\infty} \left(\frac{\partial U}{\partial r} - \frac{U}{r + R} \right)^2 + \frac{\sigma_{thnf} B_0^2 U^2}{T_\infty} + \frac{RD_B}{T_\infty} \frac{\partial T}{\partial r} \frac{\partial b}{\partial r} \\
 &+ \frac{RD_B}{b_0} \left(\frac{\partial b}{\partial r} \right)^2 + \frac{RD_C}{T_\infty} \frac{\partial T}{\partial r} \frac{\partial c}{\partial r} + \frac{RD_C}{c_0} \left(\frac{\partial c}{\partial r} \right)^2
 \end{aligned}$$

The first term represents irreversibility of heat transfer, second represents thermal radiation, third represents fluid friction, fourth represents Joule heating. Fifth, sixth, seventh, and eighth represent mass transfer. The dimensionless form of the entropy generation can be expressed as:

$$\begin{aligned}
 N_{EG}(\eta) &= A_3 H(\theta')^2 + A_3 H \frac{4}{3} Rd(\theta')^2 \\
 &+ A_5 (A_2 + K_1) \left(f'' - \frac{f'}{\eta + \beta} \right)^2 + \frac{MBr}{A_4} (f')^2 \\
 &+ (L_1 - L_2) \theta' \phi' + \frac{L_1 + L_2}{H} (\phi')^2
 \end{aligned}$$

Bejan Number, Be

$$= \frac{\text{Entropy generation due to mass and heat transfer}}{\text{Total entropy generated}}$$

Hence,

$$Be(\eta) = \frac{A_3 H(\theta')^2 + (L_1 - L_2) \theta' \phi' + \frac{L_1 + L_2}{H} (\phi')^2}{A_3 H(\theta')^2 + A_3 H \frac{4}{3} Rd(\theta')^2 + A_5 (A_2 + K_1) \left(f'' - \frac{f'}{\eta + \beta} \right)^2 + \frac{MBr}{A_4} (f')^2 + (L_1 - L_2) \theta' \phi' + \frac{L_1 + L_2}{H} (\phi')^2} \quad (22)$$

3. Numerical solution

This section discusses a numerical methodology to obtain the solution of the nondimensional higher-order coupled ODEs. For computational analysis, the Shooting procedure is a technique for solving a boundary value problem (BVP) by reducing it to an initial value problem (IVP) of first order differential equation. The obtained ODEs (13–17) and the corresponding boundary conditions (18) are solved by shooting method. Let us assume

$$\begin{aligned} Z_1 &= f; Z_2 = f'; Z_3 = f''; Z_4 = f'''; Z_5 = g; Z_6 = g'; \\ Z_7 &= \theta; Z_8 = \theta'; Z_9 = \phi; Z_{10} = \phi'; \xi = Z_6' \end{aligned} \quad (23)$$

The system of first-order differential equation is given by:

$$\left. \begin{aligned} Z_1' &= Z_2 \\ Z_2' &= Z_3 \\ Z_3' &= Z_4 \\ Z_4' &= \frac{(A_2 + K_1) \left[\frac{-2Z_4}{\eta + \beta} - \frac{Z_3}{(\eta + \beta)^2} - \frac{Z_2}{(\eta + \beta)^3} \right] - \frac{A_1 \beta}{\eta + \beta} (Z_1 Z_4 - Z_2 Z_3) - \frac{A_1 \beta}{(\eta + \beta)^2} [Z_1 Z_3 - (Z_2)^2] + \frac{A_1 \beta}{(\eta + \beta)^3} Z_1 Z_2 + K_1 \left(\xi + \frac{1}{\eta + \beta} Z_6 \right) - A_1 M \left(Z_3 + \frac{1}{\eta + \beta} Z_2 \right)}{(A_2 + K_1)} \\ Z_5' &= Z_6 \\ Z_6' &= -\frac{Z_6}{\eta + \beta} - \frac{\beta}{(\eta + \beta) \left(\frac{A_2 + 2K_1}{A_1} \right)} \left(Z_1 Z_6 - Z_2 Z_5 \right) + \frac{K_1}{A_1} \left(2Z_5 + Z_3 + \frac{Z_2}{\eta + \beta} \right) \\ Z_7' &= Z_8 \\ Z_8' &= -\frac{Z_8}{\eta + \beta} - \frac{\left[\frac{MBr}{A_4} + \frac{A_4 \beta Pr Z_1 Z_8}{\eta + \beta} + \frac{1}{A_2} Br (A_2 + K_1) \left(Z_3 - \frac{Z_2}{\eta + \beta} \right)^2 \right]}{(A_3 + \frac{4}{3} Rd)} \\ Z_9' &= Z_{10} \\ Z_{10}' &= -\frac{Z_9}{\eta + \beta} + \left[Kr_1 Z_9 (1 - Z_9)^2 - \frac{\beta Z_1 Z_{10}}{\eta + \beta} \right] Sc \end{aligned} \right\} \quad (24)$$

and the corresponding boundary conditions become:

$$\begin{aligned} Z_1(0) &= S; Z_2(0) = \lambda; Z_5(0) = -nZ_3(0); \\ Z_7(0) &= 1; Z_{10}(0) = Kr_2 Z_9(0); Z_2(\infty) = 0; \\ Z_3(\infty) &= 0; Z_5(\infty) = 0; Z_7(\infty) = 0; Z_9(\infty) = 1 \end{aligned} \quad (25)$$

BVP5C in MATLAB is used to obtain the numerical results for Eq. (20) with boundary conditions (eq. (21)). The flow chart of solution process is shown in Fig. 2.

4. Solution design

In general, there are three types of neural networks available. The first is to predict the response variable from past values of response data and past values of predictor data. The second one is to predict responses from past values of the response series itself. The third one is to predict responses from past values of another series of predictors. This study used the third network type. The η values served as the predictor data, and

$f', g, [03B8]$, and ϕ values served as the response data. During solving the ODEs (13–17), 100 data points were considered for η . Hence, the total data has 100 observations. Of these 100 observations, 80%, i.e. 80 observations, are considered for training the model, 10%, i.e. 10 observations, are considered for validation, and 10%, i.e. 10 observations, are considered for testing datasets. Values are assigned for the network parameters. Here, hidden layer of size 40 is considered. 2 min is the time delay for stopping model training. 1 layer for the input layer and 4 layers in the output layer. During the model training, the network weights for the input data are trained through the activation function used in the Bayesian regularization backpropagation. The network is illustrated in Fig. 3. The following are the stopping criteria for the model:

- The number of epochs (iterations) has crossed the upper limit of 1000 epochs.
- The time to train the model has exceeded the upper limit of 2 mins.
- The validation performance of the network has crossed the lower limit of 0.
- The performance gradient has crossed the minimum gradient value of 0.0000001.
- The algorithm Mu became greater than the maximum Mu value of 1000000000.

After training the BRBP model, it is analyzed using training state, performance, error histograms, model response, error autocorrelation, and input-error correlation plots. After solving the ODEs (13–17) using BVP5C, we get the functional solutions. After training the model, we have a trained model which incorporates those functions. These trained models can be directly used in many computer applications, can be integrated with mathematical software,

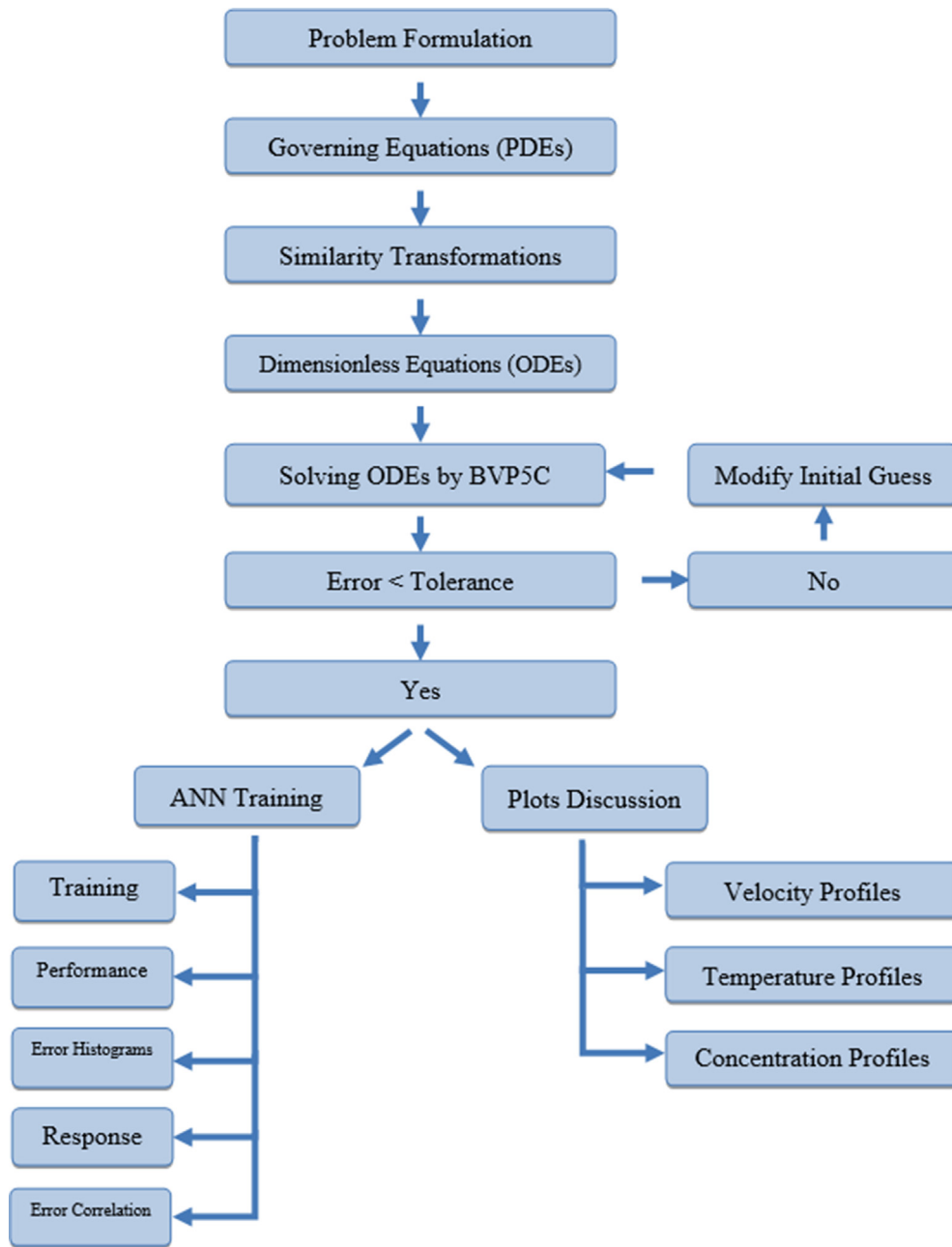


Fig. 2 Flow chart of the solution Methodology.

and have much more importance. These models provide a simple and accurate way of predicting the fluid properties. The plots used for analysis provide useful information on the performance of various models. Depending on the requirements, the best model parameters can be obtained after studying these plots. Each plot has its own importance in the analysis, which is mentioned in the individual sections ahead. Many times, we need to find solutions to complex problems, and ANN approximations play a crucial role in solving those problems. For some experiments, when we do not have the governing equations but just the experimental data, we can still use this trained model to predict the fluid properties.

5. Results validation

This section compares the present findings to previously published research. Using the appropriate assumptions, the velocity and temperature profiles of the present work are compared to those of a prior study Kottakkaran et al. [33].

Figs. 4a and 4b are used to validate the fluid problem formulated in this study. The present model is converted into an earlier published work of Kottakkaran et al. [33]. Some terms from the governing equations (13)–(17) are nullified and matched with their governing equations. From these figures, it is concluded that the results obtained in the current analysis

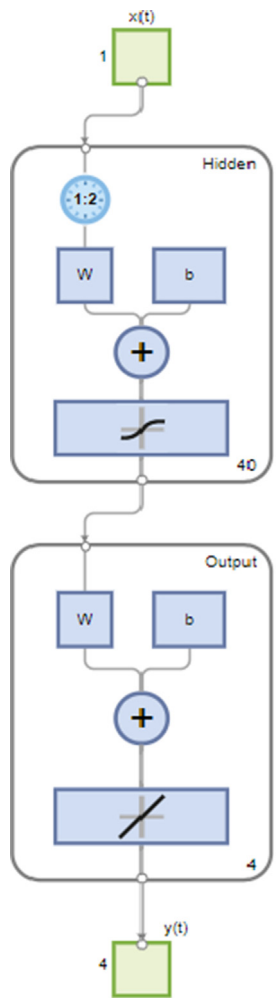


Fig. 3 ANN architecture.

are in good agreement with the study of Kottakkaran et al. [33].

Further sections highlight the importance and effects of dimensionless numbers on axial velocity, micro rotational velocity, temperature, and the concentration profiles along with suitable justifications. Table-2. contains the values used to formulate various cases. Table-3. shows the range of parameters obtained from the literature reviews. The default values used in algorithm are, $\lambda = -1$, $\beta = 2.0$, $M = 2.0$, $Rd = 8$, $Br = 0.1$, $Pr = 22$, $Sc = 0.5$, $n = 0.5$, $S = 4.5$, $K_1 = 0.05$, $Kr_1 = 0.1$, $Kr_2 = 0.01$, $\phi_{CuO} = 0.005$, $\phi_{TiO_2} = 0.005$, $\phi_{SiO_2} = 0.005$.

6. Results and discussions

To get physical insight in to the problem, a combined effects of physical parameters including curvature, micro-polar, radiation, magnetic, Prandtl, Eckert, Schmidt, and homogeneous and heterogeneous chemical reaction parameters are analyzed for velocity, micro rotational, temperature, and concentration profile. Physical quantities of engineering interest like heat transfer rate, mass transfer rate, skin friction coefficient, couple stress coefficient, and entropy generation are also discussed

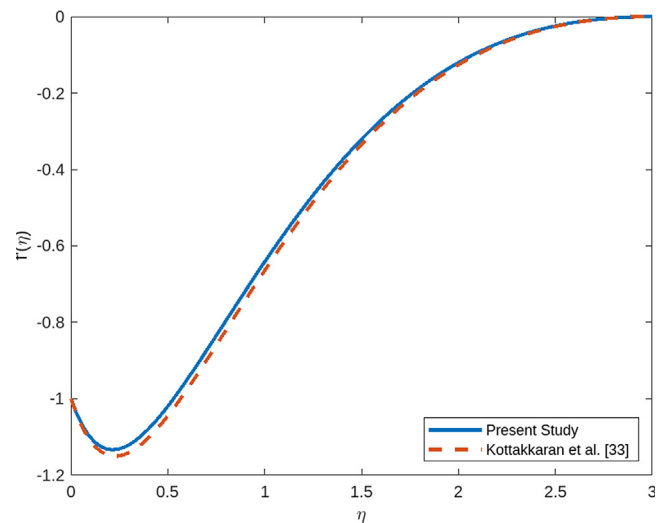


Fig. 4a Model validation for f .

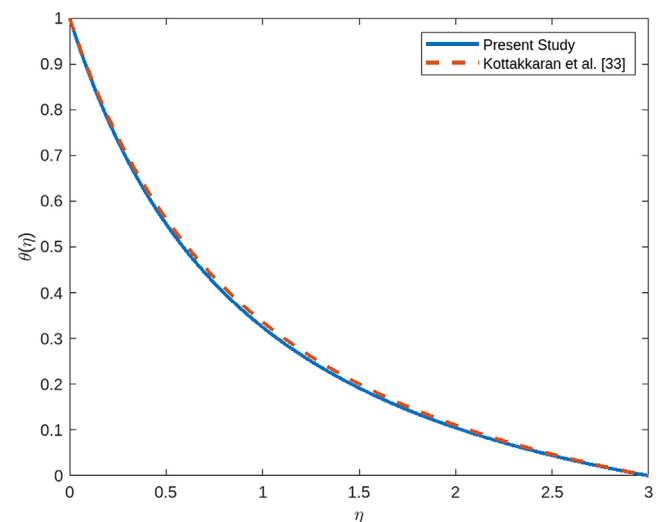


Fig. 4b Model validation for θ .

in this study. A Bayesian regularization backpropagation algorithm is also designed for the solution of the ordinary differential equations.

6.1. Effect of curvature parameter

Fig. 5a shows the effect of the radius of curvature (ROC) parameter, β on the axial velocity. It is observed that by increasing β , the axial velocity decreases. Fig. 5b shows the effect of β on the micro rotational velocity. From the figure, it can be noted that increasing the values of β , the micro rotational velocity also enhances. Physically, the radius of the stretched sheet grows as the values of β increase and there is increased resistance to fluid movement. It decreases the axial velocity and increases the rotations of nanoparticles in the base fluid [33]. Fig. 5c depicts the effect of β on the temperature. It is noticed that for enhanced values of β , the temperature profiles also enhance. Fig. 5d represents the impact of β on the concentration profiles. It shows that for larger values of β , the concentration profiles reduce. Physically, the definition of

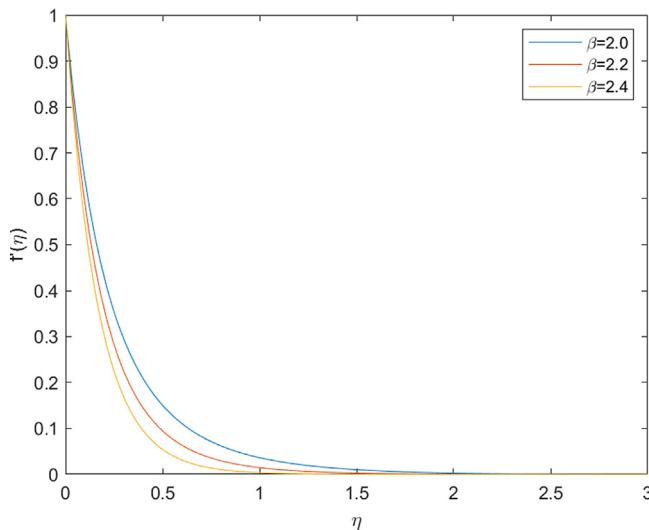


Fig. 5a Axial velocity VS Curvature parameter.

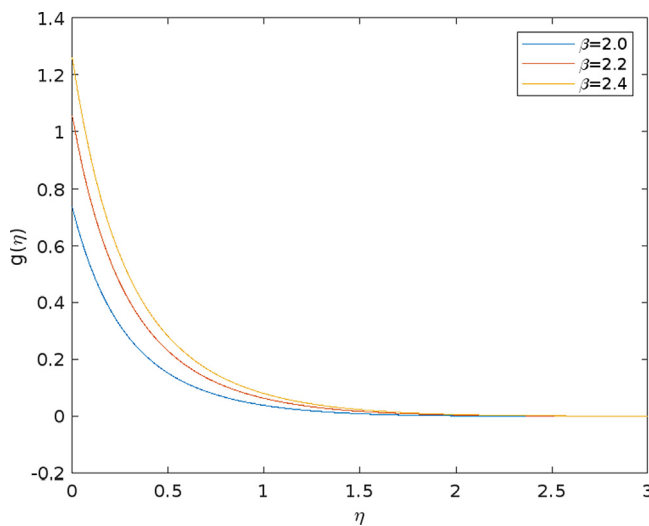


Fig. 5b Micro rotation velocity VS Curvature parameter.

β states that it has an inverse relationship with kinematic viscosity. For enhanced β , the heat generation in the base fluid boosts up and the nanoparticles' collisions and merging increase, which falls the concentration of nanoparticles.

6.2. Effect of magnetic field parameter

Fig. 6a shows the effect of the magnetic field parameter (M) on the axial velocity. The figure shows that for enhanced values of M , the axial velocity also increases. Fig. 6b depicts how larger values of M impacts the micro rotational velocity. It is observed that for larger values of M , the micro rotational velocity falls up. Physically, for larger values of M , higher Lorentz force generated. The higher Lorentz force moves the nanoparticles faster in the flow direction, increasing the fluid velocities [52]. Fig. 6c represents the effect of M on temperature distribution. It is noticed that for larger values of M , the temperature profiles decrease. Fig. 6d illustrates the impact of M on the fluid concentration. From the figure, it is observed that as M increases, the concentration profiles fall. Physically,

the larger values of M generate more Lorentz force on the nanoparticles. These nanoparticles move further from the boundary layers. Hence, the concentration and temperature decrease starting from the boundary layers.

6.3. Effect of micro polar parameter

Fig. 7a represents the effect on axial velocity for the micro rotational parameter, K_1 . Figure reveals that as the values of K_1 increase, the axial velocity rises. Fig. 7b depicts the effect of K_1 on the micro rotational velocity. For larger values of K_1 the micro rotational velocity also increases. Higher values of the micropolar parameter cause increased centrifugal forces on the curved surface. These forces boost the nanoparticles in the fluid flow direction, which causes the fluid velocities to enhance [33]. Fig. 7c represents the effect of K_1 on the temperature profiles. It is observed that for larger values of K_1 the temperature profile increases. Fig. 7d shows the influence of K_1 on the fluid concentration. It is noticed that as the values of K_1 increase, the concentration also increases. Physically, the larger generated centrifugal forces increase the amount of generated heat energy, so higher energies enhance the fluid temperature.

6.4. Effect of Radiation, Prandtl number, homogenous / heterogeneous reaction parameter

The impact of the thermal radiation parameter (R_d) and Prandtl number (Pr) on the temperature profile is depicted in Figs. 8a and 8b, respectively. It is observed that temperature profile increases with increasing radiation parameter and Prandtl number. The effect of heat radiation improves the conduction properties of the nanofluid. This happens because more heat will generate, which will enhance the thickness of the thermal boundary layer. A dominant effect for conduction is established. The system's temperature rises because of the heat released through radiation [36]. According to Fig. 8b, as Prandtl number rises, leading to larger temperature values. The Prandtl number of a fluid indicates the importance of the momentum boundary layer relative to the thermal boundary layer in terms of heat transfer. Now, as per observation from Figs. 8c and 8d, the greater homogeneous response variable Kr_1 values are associated with homogenous fluid concentrations inside the boundary layer thickness. On the other hand, a lower value of Kr_1 causes homogeneity to appear close to the surface of the bent sheet [38]. Reducing the heterogeneous reaction parameter Kr_2 increases the reaction rate at the plate surface. For both homogeneous and heterogeneous reaction parameters, the concentration is observed to be declining.

6.5. Effect of concentration of nanoparticles

Fig. 9a shows the effect of nanoparticle concentration of CuO on axial velocity. The figure reveals that by increasing the CuO concentration, the axial velocity increases. Physically, the presence of nanoparticles enhances the viscosity of the fluid, resulting in reduced frictional losses and improved flow characteristics. This reduced viscosity leads to lower internal resistance, allowing for higher fluid axial velocities. Fig. 9b depicts the effect of increasing nanoparticle concentration of

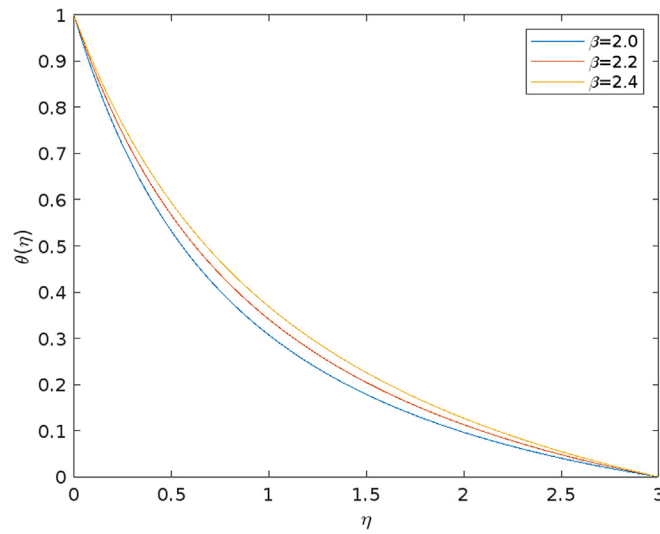


Fig. 5c Temperature VS Curvature parameter.

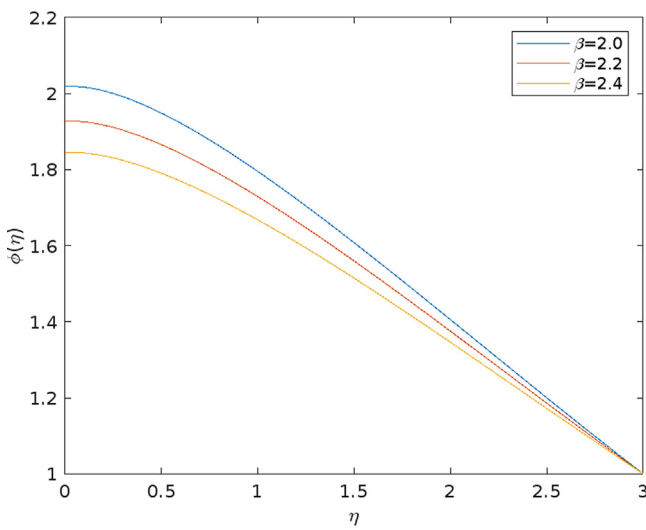


Fig. 5d Concentration VS Curvature parameter.

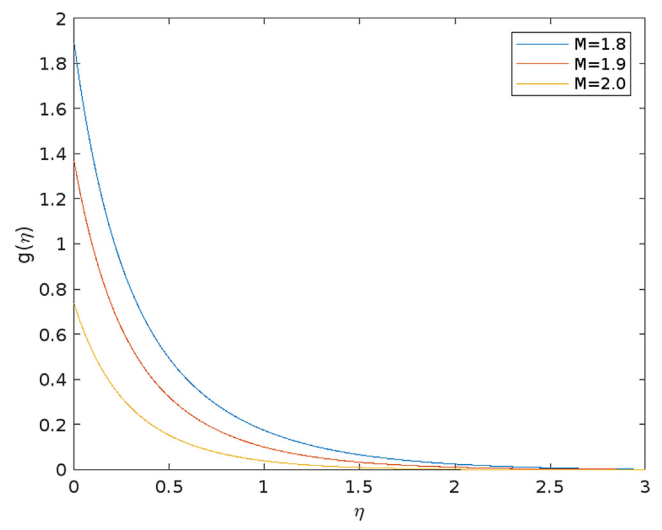


Fig. 6b Micro rotation velocity VS Magnetic field parameter.

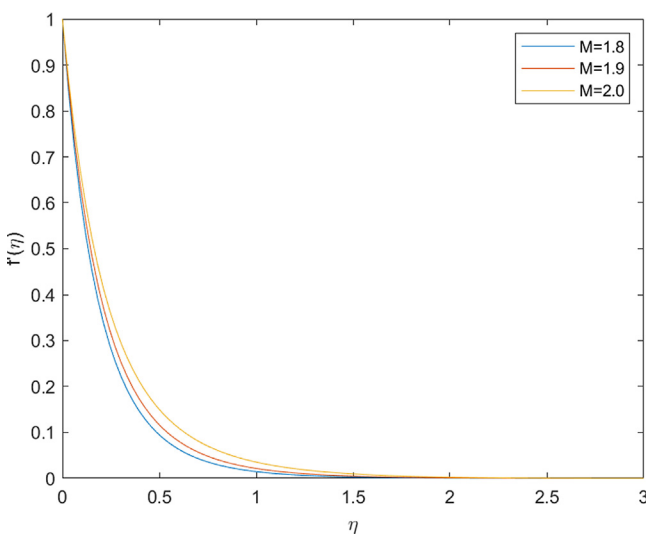


Fig. 6a Axial velocity VS Magnetic field parameter.

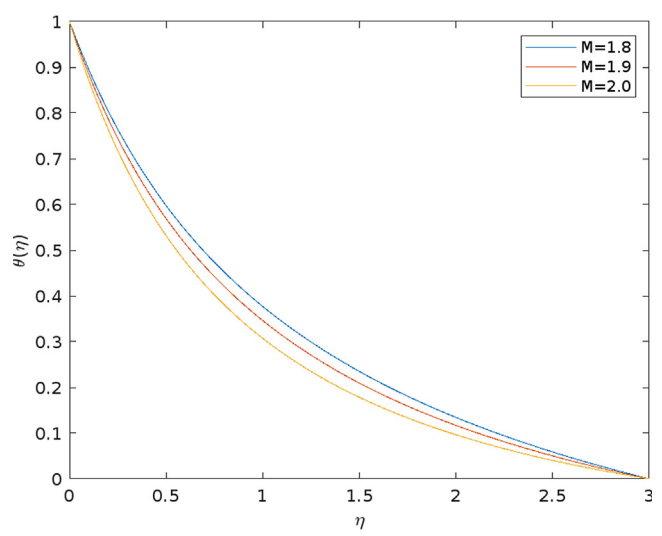


Fig. 6c Temperature VS Magnetic field parameter.

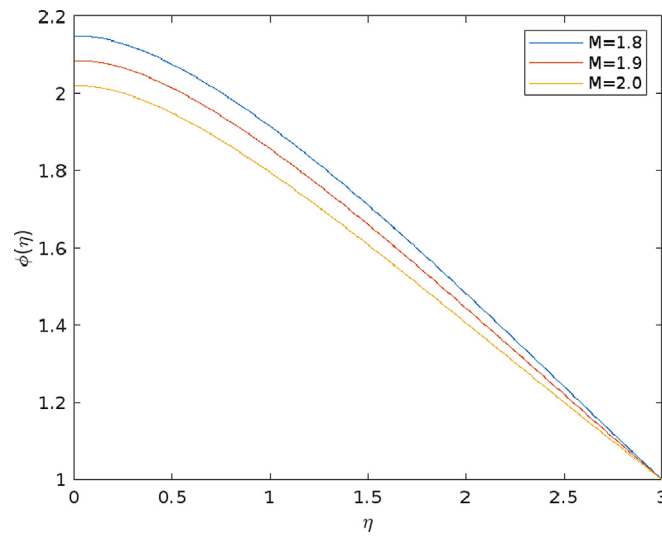


Fig. 6d Concentration VS Magnetic field parameter.

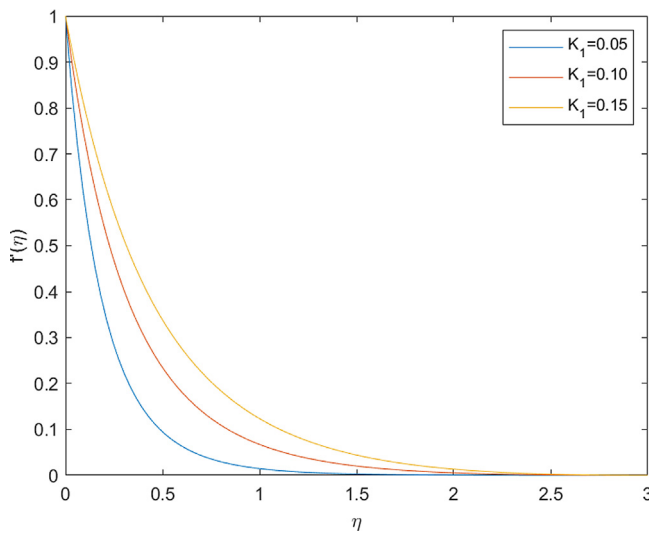


Fig. 7a Axial velocity VS Micro polar parameter.

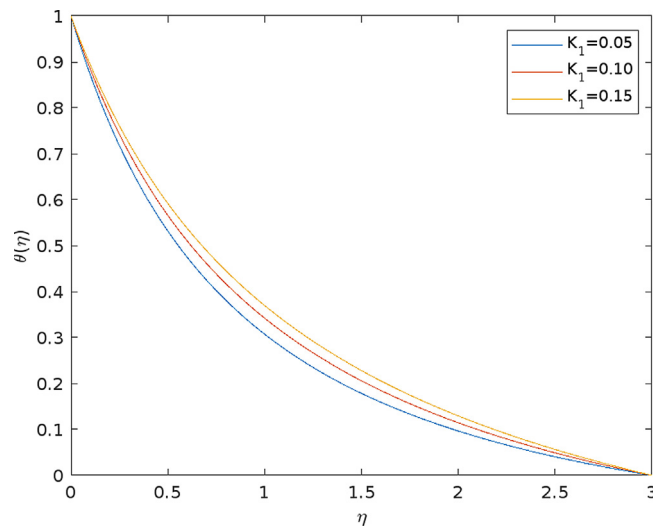


Fig. 7c Temperature VS Micro polar parameter.

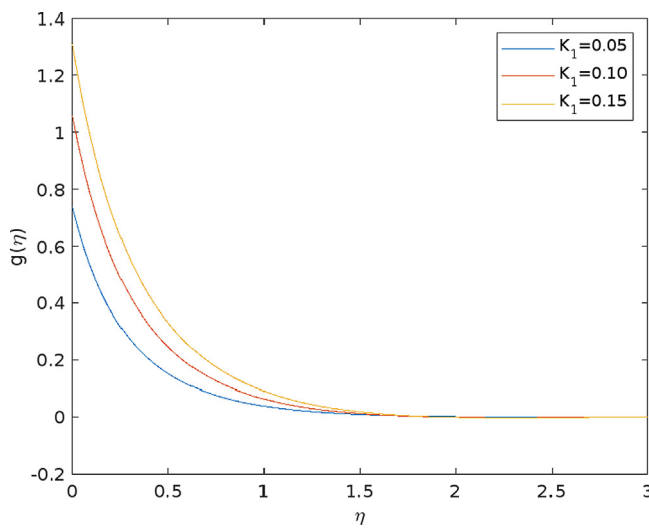


Fig. 7b Micro rotation velocity VS Micro polar parameter.

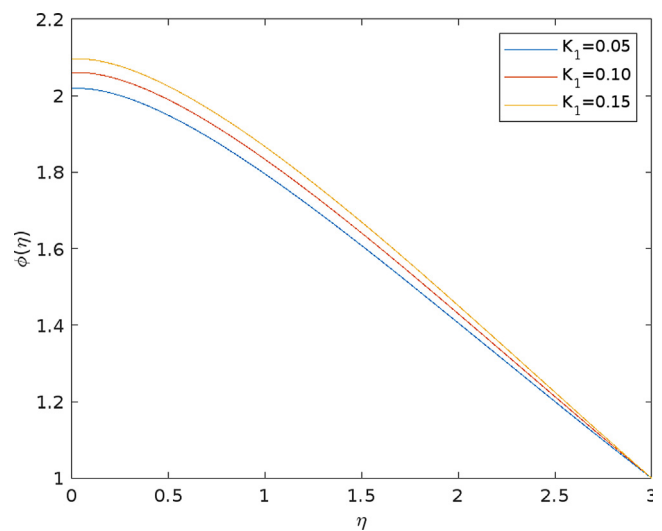


Fig. 7d Concentration VS Micro polar parameter.

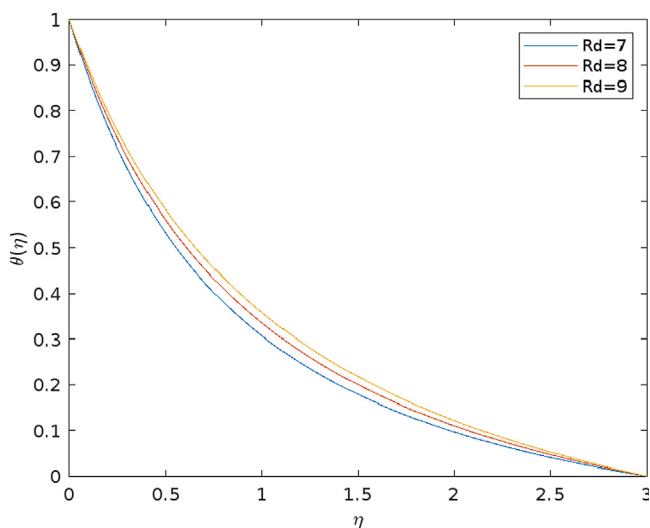


Fig. 8a Temperature VS Thermal radiations parameter.

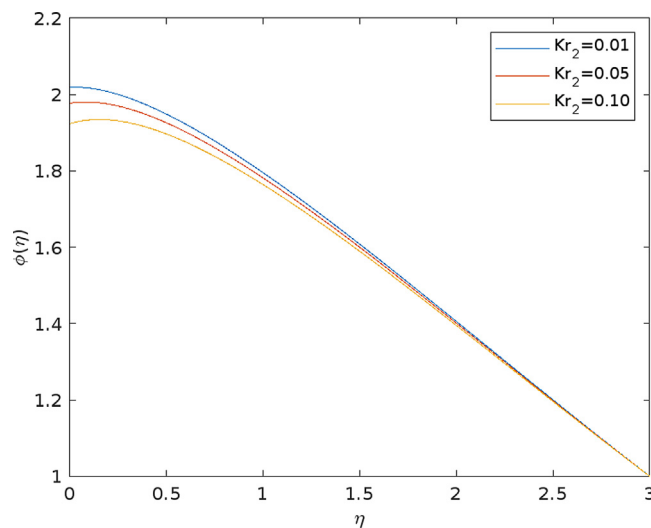


Fig. 8d Concentration VS Heterogeneous reaction parameter.

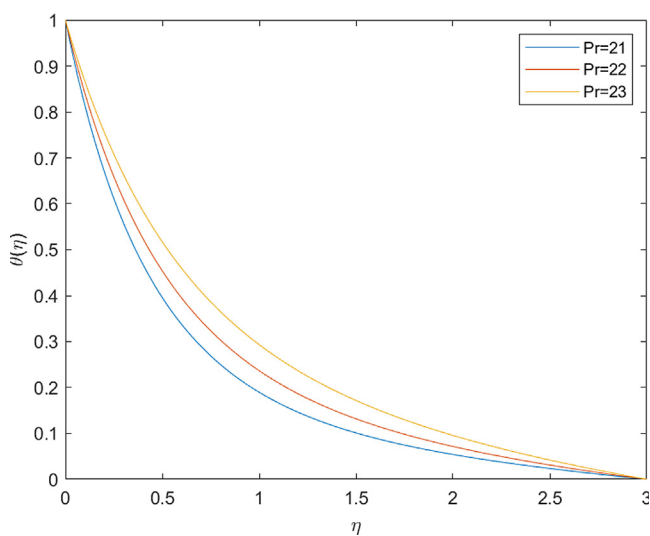


Fig. 8b Temperature VS Prandtl number.

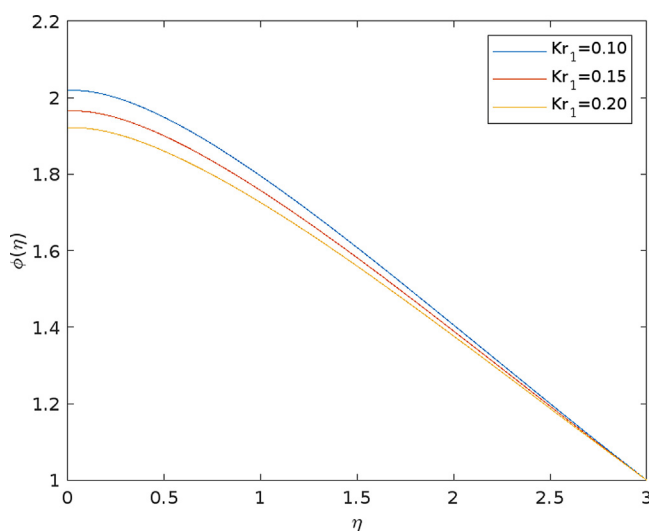


Fig. 8c Concentration VS Homogeneous reaction parameter.

CuO on micro rotational velocity. For enhanced CuO concentration, the micro rotational velocity decreases. The higher concentration of nanoparticles leads to stronger intermolecular interactions and a thicker boundary layer, resulting in reduced fluid mobility and hindered rotational movement [55].

Fig. 9c illustrates the impact of CuO concentration on the fluid concentration. The figure shows that for higher concentration of CuO, the fluid concentration decreases. By increasing the concentration of TiO₂, negligible change is observed in velocities and concentration. However, the temperature profile decreases, as shown in Fig. 9d. Nanoparticles have high thermal conductivity compared to the base fluid, and as their concentration increases, nanoparticles act as conductive pathways for heat transfer. This leads to more efficient heat dissipation from the fluid, resulting in a decrease in the base fluid temperature. Fig. 9e illustrates the impact of increased SiO₂ concentration on the axial velocity. It is observed that by enhancing the SiO₂ concentration, the axial velocity decreases. SiO₂ has a higher viscosity compared to the base fluid, and as

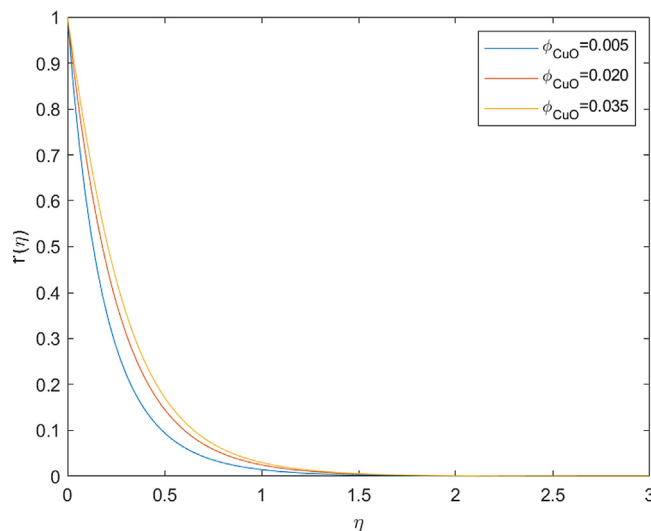


Fig. 9a Axial velocity VS CuO concentration.

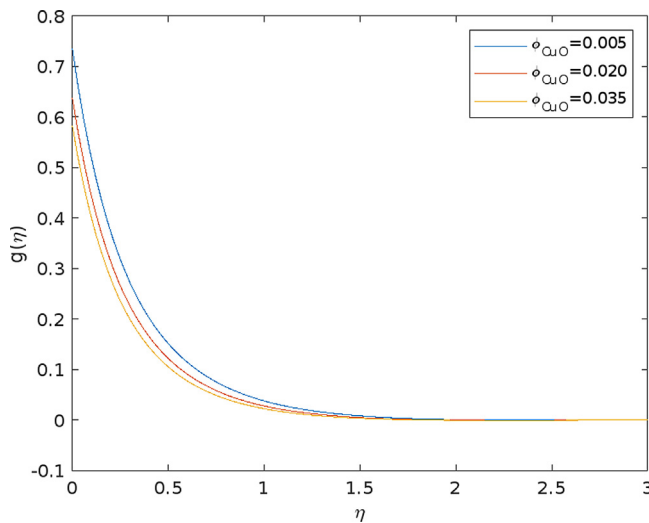


Fig. 9b Micro rotation velocity VS CuO concentration.

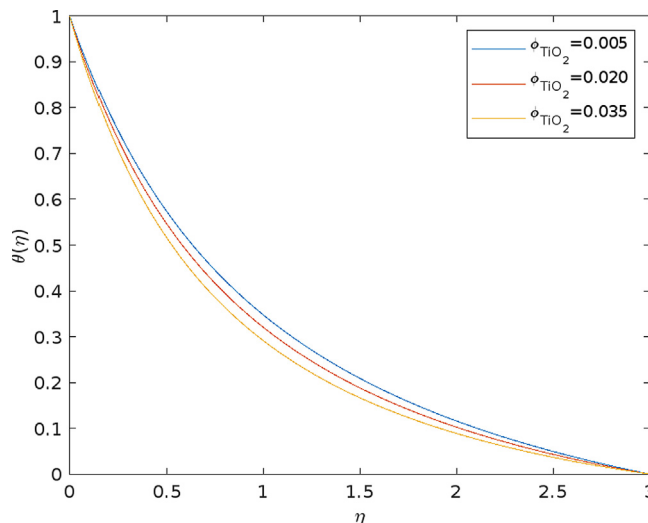


Fig. 9d Temperature VS TiO₂ concentration.

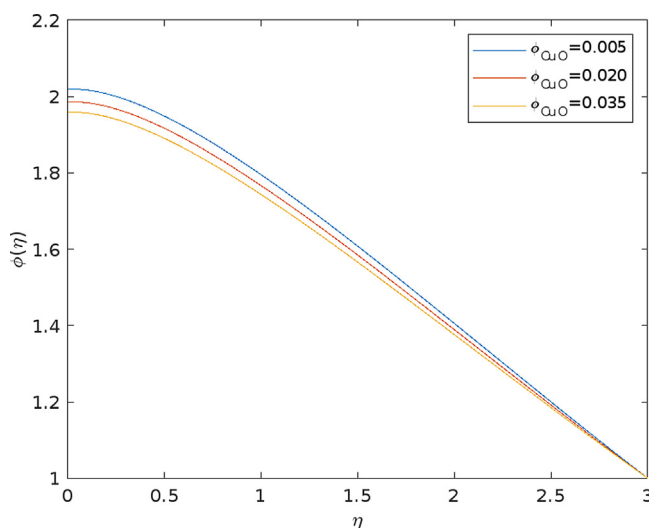


Fig. 9c Concentration VS CuO concentration.

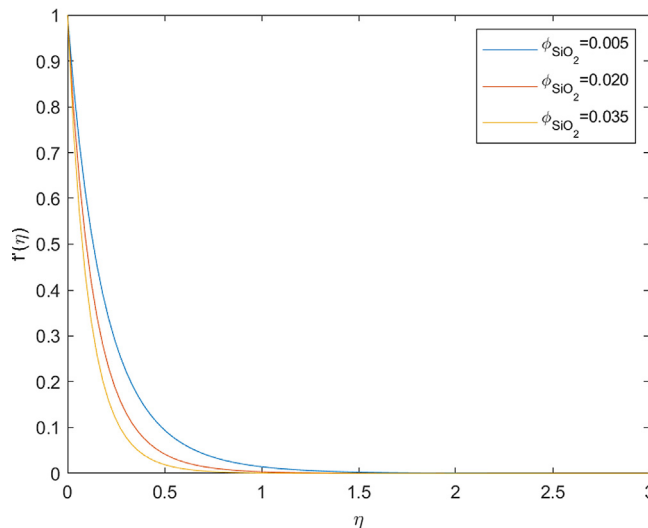


Fig. 9e Axial velocity VS SiO₂ concentration.

its concentration increases, the overall viscosity of the fluid increases as well. Fig. 9f shows the impact of increased SiO₂ concentration on the micro rotational velocity. On enhancing the SiO₂ concentration, the micro rotational velocity improves. As the SiO₂ concentration increases, the fluid's viscosity tends to increase, resulting in higher resistance to shear forces. This increased resistance can cause the fluid to rotate or swirl more vigorously, leading to an increase in micro rotational velocity [55]. Figs. 9g and 9h show the effect of SiO₂ concentration on temperature and concentration profiles. Temperature and concentration profiles rise with increased SiO₂ concentration due to enhanced heat transfer and particle density. Fig. 9g. Fig. 9h.

6.6. Bayesian regularization backpropagation algorithm graphical analytics

After getting the solutions of the ODEs (13–17) for 100 values of η , ANN is trained using the Bayesian regularization back-

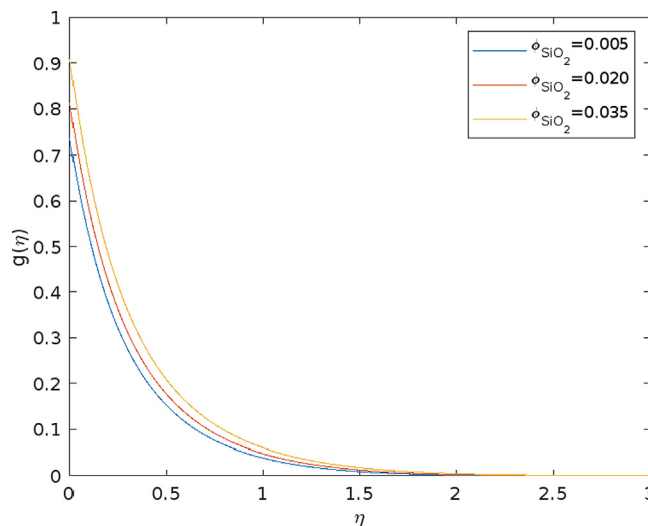


Fig. 9f Micro rotation velocity VS SiO₂ concentration.

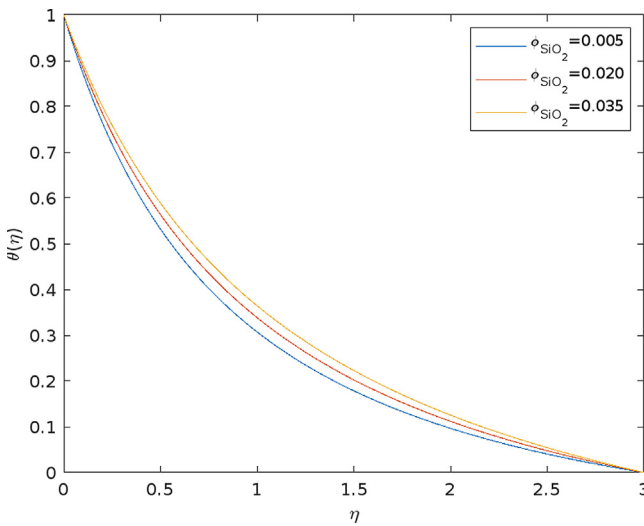


Fig. 9 g Temperature VS SiO₂ concentration.

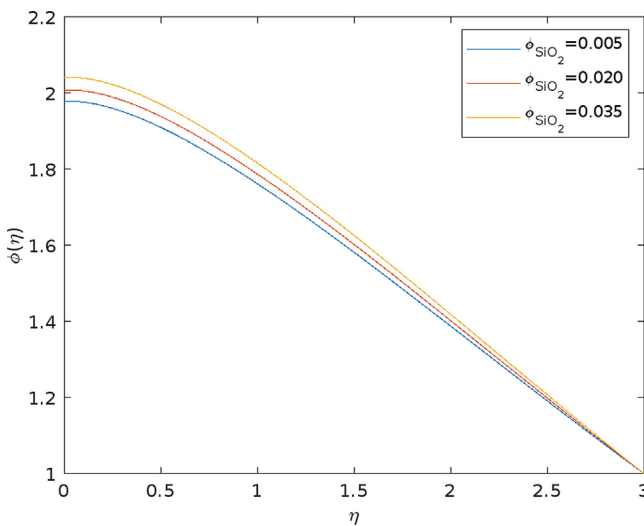


Fig. 9 h Concentration VS SiO₂ concentration.

propagation algorithm for the axial velocity, micro rotational velocity, temperature, and concentration. This trained network consists of data points obtained from the default values of the dimensionless numbers. Fig. 10a shows the training state of the model from the 0th epoch to the final epoch (668). In the backpropagation algorithm, the weights are trained as a function of the partial derivatives of error with respect to the weights and the learning rate, and the gradient plays an important role in training. The figure shows the gradient values for each epoch; at the final epoch, the gradient comes out to be 7.2084e-08.

The learning rate or Mu has a value of 50,000 at the 668th epoch. At the 668th epoch, the numerical parameter has a value of 67.0994, and the sum of the squared parameter has a value of 341.1405. Validation failures happen when the validation error in the validation dataset crosses the upper limit. The figure shows that there were no validation failures. Hence, the model was trained well for all the epochs. Fig. 10b shows the best training performance of the model epoch-wise. It can be seen that, while training the model, the training and the testing errors reduced till the final epoch as the model stopped training due to the stopping criteria of the gradient. The best training performance is achieved at the 668th epoch of 5.5766e-12.

Fig. 10c shows the error histogram of the model. It is obtained by considering several random samples in training, testing, and validation datasets. The sample data used in the model are compared between the predicted and the actual values. The error obtained is converted into 20 bins. The X-axis shows those 20 bins for 0–400 instances (samples) represented on the Y-axis. The figure shows that most of the samples got zero error (orange line). Fig. 10d shows the response plot of the model. The model predicted training, validation, testing values, and all data. The figure shows how well the model fits the data and the obtained errors. The bottom plot shows the error concerning the training time. It can be seen that the major error occurred at the start only.

Fig. 10e shows the autocorrelation of errors. The autocorrelation plot shows the relationship between the prediction errors and time. The autocorrelation function should have only one nonzero value for a decent model and take place at

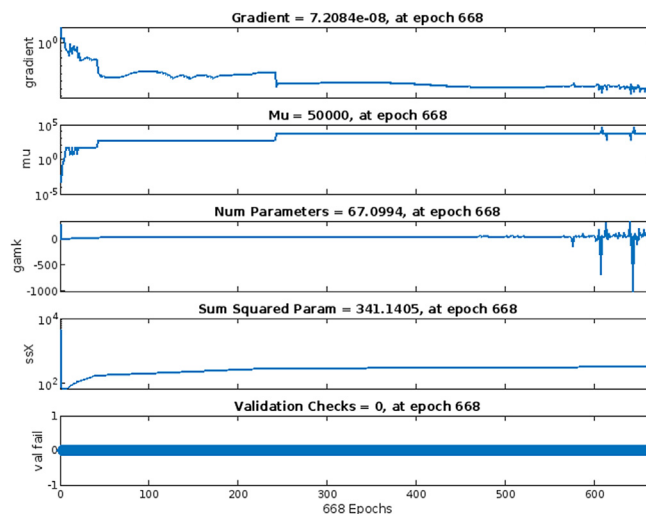


Fig. 10a Training state plot.

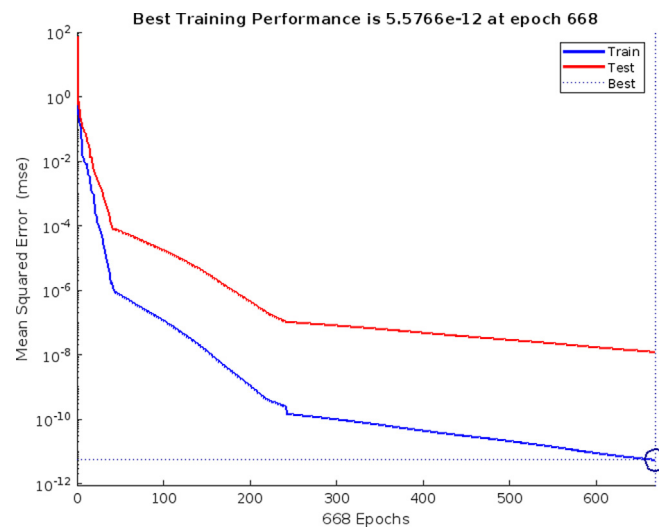


Fig. 10b Best training performance plot.

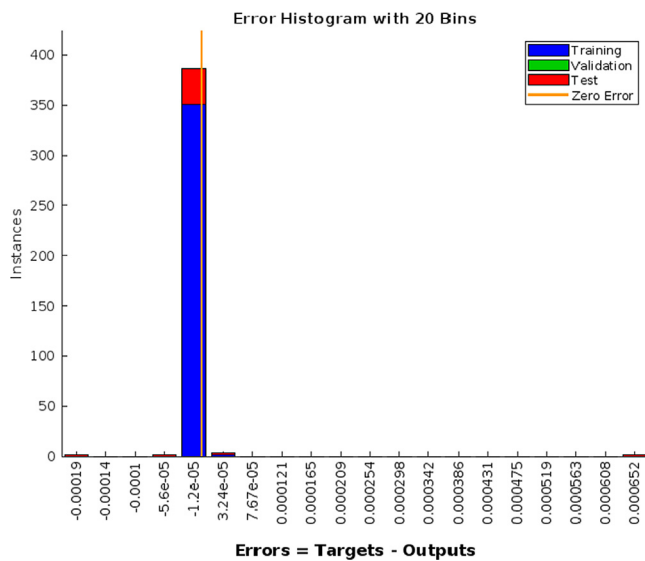


Fig. 10c Error histogram plot.

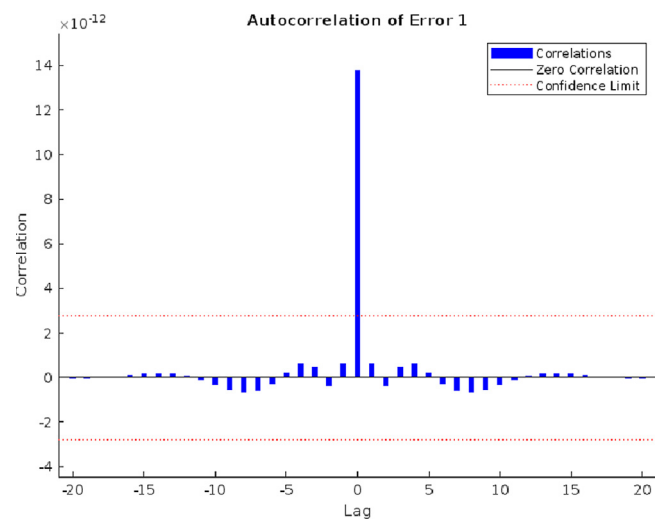


Fig. 10e Error autocorrelation plot.

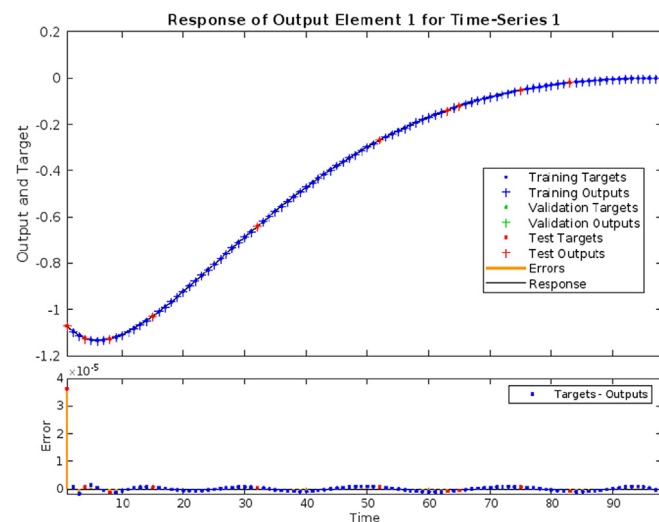


Fig. 10d Model response plot.

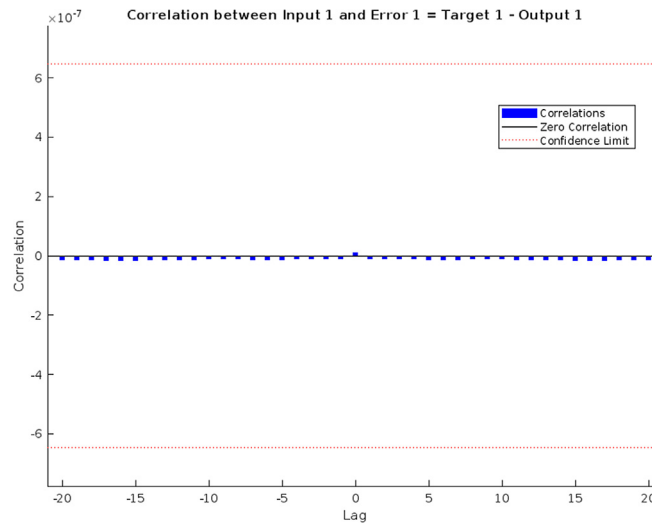


Fig. 10f Input-Error Correlation plot.

zero lag (the mean square error). This would imply that there is zero correlation between the prediction errors. It should enhance the prediction if there is a substantial correlation in the prediction errors, perhaps by adding more delays to the tapped delay lines. The correlations in this instance, except for the one at zero lag, fall roughly within the 95% confidence interval around zero, suggesting that the model is sufficient. Fig. 10f shows the Input-Error correlation plot of the model. The input-error cross-correlation figure shows the relationship between the input sequence and the errors. All correlations should be zero in a good model. If the input is correlated with the error, improving the prediction by increasing the number of delays in the tapped delay lines should be possible. Most correlations in this situation are contained by the confidence intervals surrounding zero. As a result, the model fits the data well.

6.7. Entropy generation and Bejan number

Entropy generation plays a significant role in blood flow by providing insights into the irreversible processes and energy dissipation occurring within the system. In the context of thermodynamics, entropy generation quantifies the degree of irreversibility or disorder in a process. In the case of blood flow, it represents the inefficiencies and losses associated with the transport of blood through the circulatory system. Physically, entropy generation in blood flow arises due to various factors. One of the primary contributors is the frictional resistance encountered as blood flows through the blood vessels. This frictional resistance, known as viscous dissipation, results in the conversion of mechanical energy into heat called Joule heating. Additionally, other forms of dissipation, such as heat transfer between the blood and surrounding tissues, chemical reactions, and fluid mixing, contribute to entropy generation.

The entropy generation and Bejan number profiles for thermal radiation and the Brinkman number ($Br = Pr \cdot Ec$) are shown in Figure 11. Prandtl number controls how thick the thermal and momentum boundary layers are in comparison. Smaller Pr values result in faster heat diffusion from the heated

surface than larger Pr values because thermal conductivity rises as Pr falls. The intensification of the Eckert number causes the drag force between the liquid's particles to grow, which speeds up heat transfer or raises the fluid's entropy. The Eckert number refers to the link between kinetic energy and the fluctuation in heat enthalpy. As a result, the hybrid nanofluid's kinetic energy rises as Ec increases. The average kinetic energy is considered in relation to temperature. As a result, raising the Br causes increment in entropy generation (Fig. 11a) and the Bejan number (Fig. 11b) of the ternary hybrid nanofluid. Figs. 11c and 11d depict that the entropy generation and Bejan number increase by increasing Rd. Physically, greater values of Rd have dominant effects over conduction. Therefore, due to radiation a good amount of heat is released in the system, which raises the temperature.

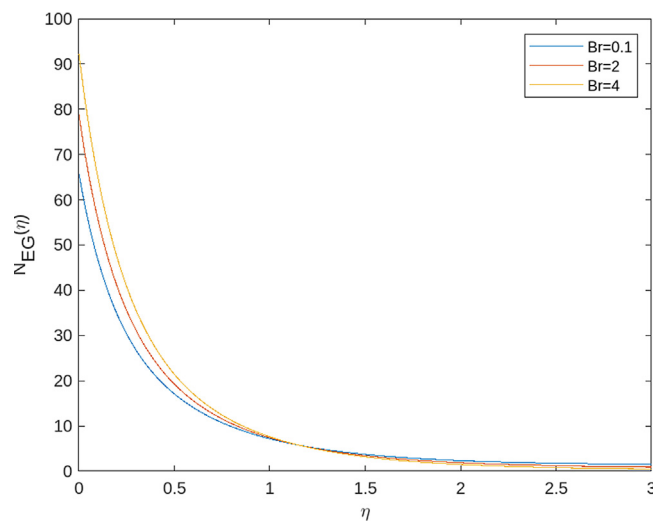


Fig. 11a Entropy generation VS Brinkman number.

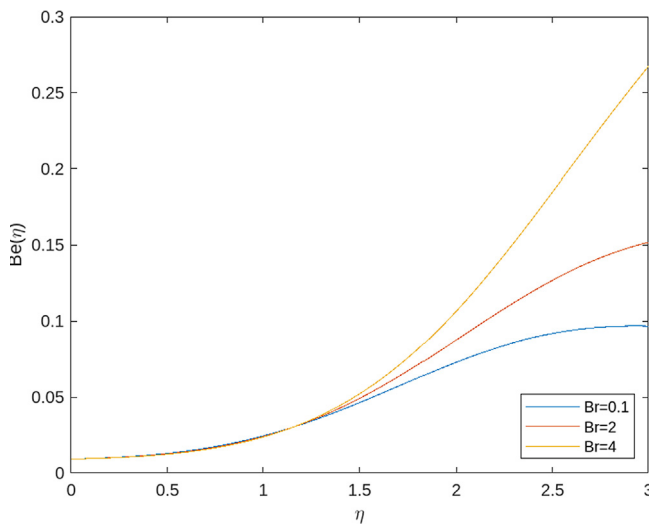


Fig. 11b Bejan number VS Brinkman number.

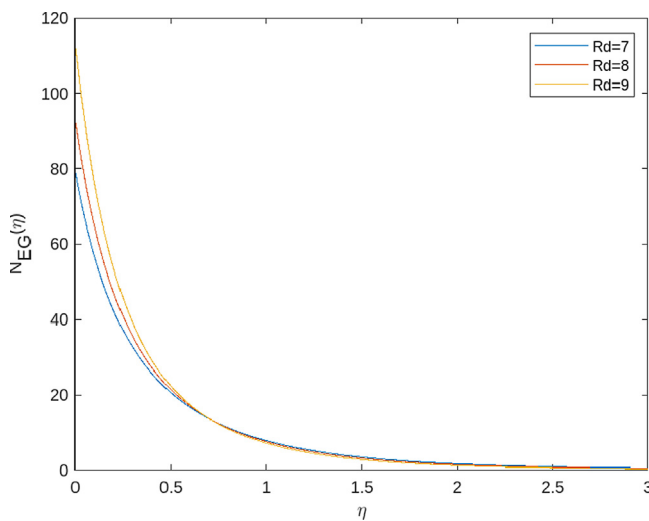


Fig. 11c Entropy generation VS Radiation parameter.

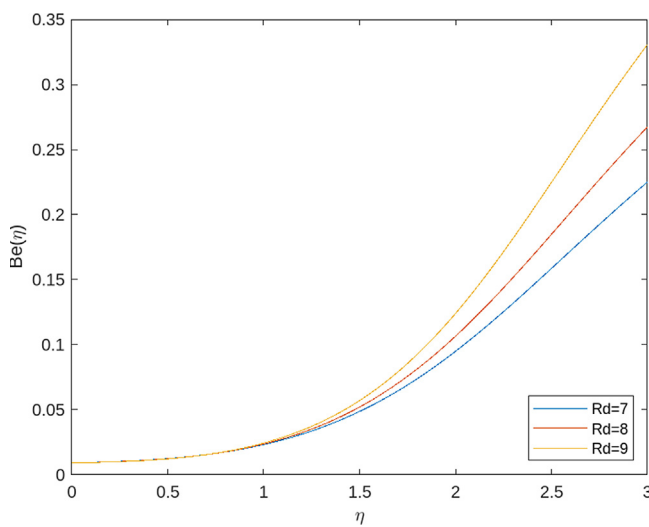


Fig. 11d Bejan number VS Radiation parameter.

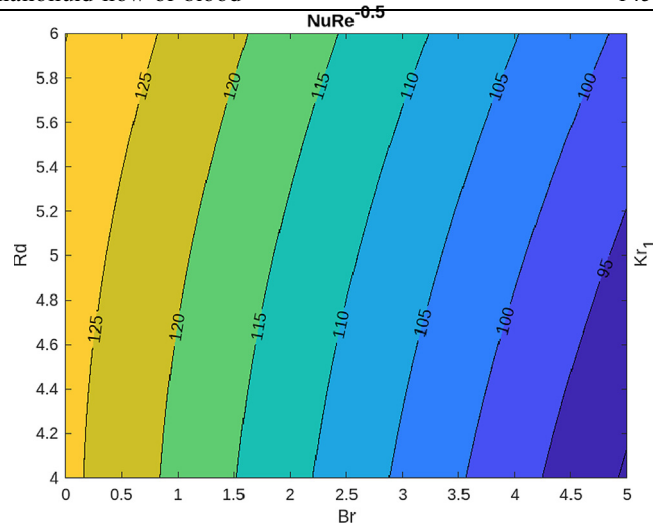


Fig. 12a Brinkman number VS Radiation parameter VS Nusselt number.

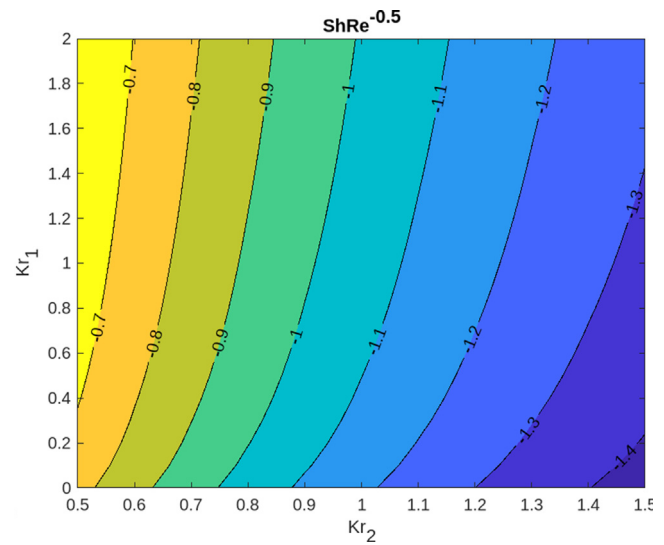


Fig. 12b Homogeneous VS Heterogeneous VS Sherwood number.

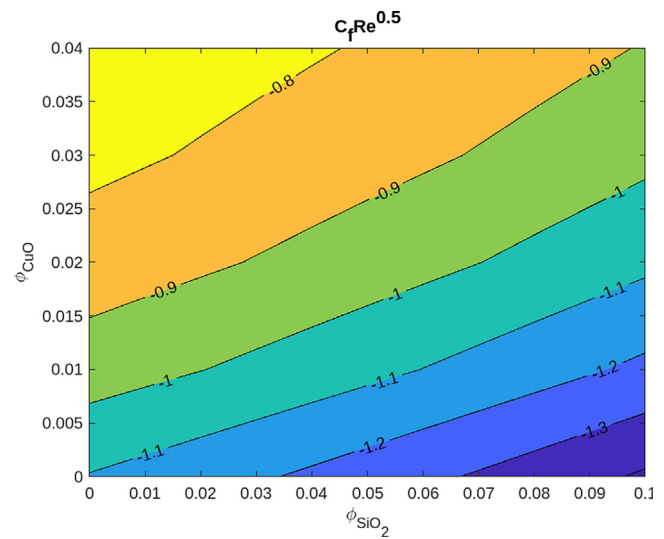


Fig. 12c SiO_2 concentration VS CuO concentration VS Skin friction coefficient.

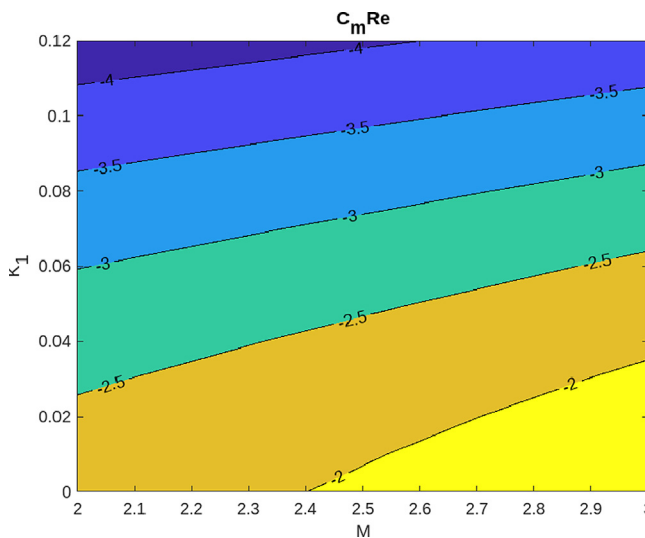


Fig. 12d Magnetic number VS Micro polar parameter VS couple stress coefficient.

6.8. Nusselt number, Sherwood number, skin friction and couple stress coefficients

Figure 12 shows the contour plots for Nusselt number, Sherwood number, skin friction coefficient, and couple stress coefficient. Fig. 12a depicts that the heat transfer rate decreases by increasing the values of Br . It is noted that as increasing Rd , the Nusselt number increases. Fig. 12b illustrates that by increasing the values of Kr_1 , the Sherwood number increases, while opposite trend is observed for Kr_2 . Fig. 12c shows that on increasing the ϕ_{CuO} , the skin friction coefficient increases, and by increasing the ϕ_{SiO_2} , the skin friction coefficient decreases. Fig. 12d reveals that, by increasing the values of K_1 , the couple stress coefficient decreases, while reverse effect is noticed for M .

7. Conclusion

The study investigates the ternary hybrid nanofluid consisting of nanoparticles of titanium oxide (TiO_2), copper oxide (CuO), and silicon oxide (SiO_2) with Blood as the base fluid for a combined effect of thermal radiation, external magnetic field, homogeneous and heterogeneous chemical reactions, Joule heating, and viscous dissipation. Velocity, temperature, and concentration profiles of the ternary hybrid nanofluid are discussed graphically with proper justifications.

The important results from the study are as follows:

- The axial velocity increases by decreasing the curvature parameter, the micro polar parameter, and the silicon oxide concentration.
- The micro rotational velocity increases by increasing the curvature parameter, the micro polar parameter, and decreasing with the magnetic parameter and the copper oxide concentration.
- The temperature profiles increase by increasing curvature parameter, radiation number, Prandtl number, while decreasing with magnetic number, micro polar parameter, and titanium oxide concentration.

- The concentration profiles increase by reducing the curvature parameter, the magnetic number, homogenous and heterogeneous reaction numbers, while, opposite trend is observed with the micro polar parameter.
- The mass transfer rate increases by increasing the homogeneous reaction parameter and reducing with the heterogeneous reaction parameter.
- The heat transfer rate increases by increasing the radiation parameter, while, reverse effect is observed for Brinkman number.
- The skin friction coefficient increases the concentration of copper oxide and decreases with silicon oxide concentration. The couple stress coefficient increases for reducing micro polar parameter and rising with magnetic parameter.
- The entropy generation and the Bejan number increase for enhancing Brinkman and radiation parameter.

Understanding the flow behavior of blood is crucial in medical research, especially when considering the effects of nanofluids and reactions. This study provides insights into the behavior of micropolar ternary hybrid nanofluid flow in blood, which can contribute to the development of new medical treatments and interventions. Bayesian regularization networks enable the development of predictive models for the flow behavior and optimization of entropy generation. This model can provide insights into the efficiency and effectiveness of the fluid flow, allowing for the identification of optimal operating conditions and design parameters. Entropy generation optimization has implications for various areas, including biomedical engineering and healthcare. Understanding the flow behavior of blood and optimizing entropy generation can contribute to the design of more efficient biomedical devices, such as blood pumps, artificial organs, and drug delivery systems. It can also aid in the development of targeted therapies and diagnostics by providing insights into the transport and distribution of nanoparticles in blood.

8. Limitations of the study:

- The study makes certain assumptions regarding the flow behavior, such as the micropolar fluid model, homogeneous and heterogeneous chemical reactions, and the use of Bayesian regularization networks. These assumptions may simplify the problem and may not fully capture the complexity of the real-world blood flow behavior, which can limit the generalizability of the results.
- The magnetic Reynold's number is considered very small ($Re \ll 1$) so that the induced magnetic field can be neglected compared to the applied external uniform magnetic field.
- The study considers simplified geometries and boundary conditions, which may not fully represent the actual blood flow scenarios. Real blood flow is highly complex, occurring in intricate vasculature networks with varying geometry and boundary conditions. Neglecting such complexities may limit the applicability of the results to real-world scenarios.

Declaration of Competing Interest

The authors declare that they have no known competing financial interests or personal relationships that could have appeared to influence the work reported in this paper.

Acknowledgement

The author BKS expresses his sincere thanks to DST-SERB, New Delhi, for providing research facilities (Award letter No: MTR/2022/000315) under the MATRICS scheme. The work of U.F.-G. was supported by the government of the Basque Country for the ELKARTEK21/10 KK-2021/00014 and ELKARTEK22/85 research programs, respectively.

References

- [1] M.Y. Rafiq, Z. Abbas, M.Z. Ullah, Peristaltic mechanism of couple stress nanomaterial in a tapered channel, *Ain Shams Eng. J.* 13 (6) (2022) 101779.
- [2] M.P. Yadav, R. Agarwal, S.D. Purohit, D. Kumar, D.L. Suthar, Groundwater flow in karstic aquifer: analytic solution of dual-porosity fractional model to simulate groundwater flow, *Applied Mathematics in Science and Engineering* 30 (1) (2022) 598–608.
- [3] T. Gul, B. Ali, W. Alghamdi, S. Nasir, A. Saeed, P. Kumam, M. Jawad, Mixed convection stagnation point flow of the blood based hybrid nanofluid around a rotating sphere, *Sci. Rep.* 11 (1) (2021) 7460.
- [4] A. Saeed, A. Alsubie, P. Kumam, S. Nasir, T. Gul, W. Kumam, Blood based hybrid nanofluid flow together with electromagnetic field and couple stresses, *Sci. Rep.* 11 (1) (2021) 12865.
- [5] A.S. Alnahdi, S. Nasir, T. Gul, Blood-based ternary hybrid nanofluid flow-through perforated capillary for the applications of drug delivery, *Waves Random Complex Media* (2022) 1–19.
- [6] A. Saeed, R.A. Shah, M.S. Khan, U. Fernandez-Gamiz, M.Z. Bani-Fwaz, S. Noeiaghdam, A.M. Galal, Theoretical analysis of unsteady squeezing nanofluid flow with physical properties, *Math. Biosci. Eng.* 19 (10) (2022) 10176–10191.
- [7] Khan, M. S., Mei, S., Shabnam, Fernandez-Gamiz, U., Noeiaghdam, S., Khan, A., & Shah, S. A. (2022). Electroviscous effect of water-base nanofluid flow between two parallel disks with suction/injection effect. *Mathematics*, 10(6), 956.
- [8] Khan, M. S., Mei, S., Shabnam, Fernandez-Gamiz, U., Noeiaghdam, S., & Khan, A. (2022). Numerical simulation of a time-dependent electroviscous and hybrid nanofluid with Darcy-Forchheimer effect between squeezing plates. *Nanomaterials*, 12(5), 876.
- [9] M.F. Javed, M.I. Khan, N.B. Khan, R. Muhammad, M.U. Rehman, S.W. Khan, T.A. Khan, Axisymmetric flow of Casson fluid by a swirling cylinder, *Results Phys.* 9 (2018) 1250–1255.
- [10] P.K. Dadheech, P. Agrawal, A. Sharma, K.S. Nisar, S.D. Purohit, Transportation of Al₂O₃-SiO₂-TiO₂ modified nanofluid over an exponentially stretching surface with inclined magnetohydrodynamic, *Therm. Sci.* 25 (Spec. issue 2) (2021) 279–285.
- [11] P. Agrawal, P.K. Dadheech, R.N. Jat, K.S. Nisar, M. Bohra, S. D. Purohit, Magneto Marangoni flow of γ -AL₂O₃ nanofluids with thermal radiation and heat source/sink effects over a stretching surface embedded in porous medium, *Case Studies in Thermal Engineering* 23 (2021) 100802.
- [12] P.K. Dadheech, P. Agrawal, A. Sharma, K.S. Nisar, S.D. Purohit, Marangoni convection flow of γ -Al₂O₃ nanofluids past a porous stretching surface with thermal radiation effect in the presence of an inclined magnetic field, *Heat Transfer* 51 (1) (2022) 534–550.
- [13] S. Dinarvand, H. Berrehal, H. Tamim, G. Sowmya, S. Noeiaghdam, M. Abdollahzadeh, Squeezing flow of aqueous CNTs-Fe₃O₄ hybrid nanofluid through mass-based approach: Effect of heat source/sink, nanoparticle shape, and an oblique magnetic field, *Results in Engineering* 17 (2023) 100976.
- [14] M.S. Khan, S. Mei, U. Fernandez-Gamiz, S. Noeiaghdam, S.A. Shah, A. Khan, Numerical analysis of unsteady hybrid nanofluid flow comprising CNTs-ferrous oxide/water with variable magnetic field, *Nanomaterials* 12 (2) (2022) 180.
- [15] M.Y. Rafiq, Z. Abbas, J. Hasnain, Theoretical exploration of thermal transportation with Lorentz force for fourth-grade fluid model obeying peristaltic mechanism, *Arab. J. Sci. Eng.* 46 (2021) 12391–12404.
- [16] F. Rehman, M.I. Khan, M. Sadiq, A. Malook, MHD flow of carbon in micropolar nanofluid with convective heat transfer in the rotating frame, *J. Mol. Liq.* 231 (2017) 353–363.
- [17] A. Kumar, B.K. Sharma, R. Gandhi, N.K. Mishra, M.M. Bhatti, Response surface optimization for the electromagnetohydrodynamic Cu-polyvinyl alcohol/water Jeffrey nanofluid flow with an exponential heat source, *J. Magn. Magn. Mater.* 170751 (2023).
- [18] G. Dharmiaiah, S. Dinarvand, J.R. Prasad, S. Noeiaghdam, M. Abdollahzadeh, Non-homogeneous two-component buongiorno model for nanofluid flow toward Howarth's wavy cylinder with activation energy. *Results, Engineering* 100879 (2023).
- [19] G. Dharmiaiah, S. Dinarvand, P. Durgaprasad, S. Noeiaghdam, Arrhenius activation energy of tangent hyperbolic nanofluid over a cone with radiation absorption, *Results in Engineering* 16 (2022) 100745.
- [20] Z. Abbas, S. Hussain, M.Y. Rafiq, J. Hasnain, Oscillatory slip flow of Fe₃O₄ and Al₂O₃ nanoparticles in a vertical porous channel using Darcy's law with thermal radiation, *Heat Transfer* 49 (6) (2020) 3228–3245.
- [21] Z. Abbas, M.Y. Rafiq, J. Hasnain, T. Javed, Peristaltic transport of a Casson fluid in a non-uniform inclined tube with Rosseland approximation and wall properties, *Arab. J. Sci. Eng.* 46 (2021) 1997–2007.
- [22] Z. Shah, M. Rooman, M. Shutaywi, Computational analysis of radiative engine oil-based Prandtl-Eyring hybrid nanofluid flow with variable heat transfer using the Cattaneo-Christov heat flux model, *RSC Adv.* 13 (6) (2023) 3552–3560.
- [23] T.Q. Tang, M. Rooman, Z. Shah, M.A. Jan, N. Vrinceanu, M. Racheriu, Computational study and characteristics of magnetized gold-blood Oldroyd-B nanofluid flow and heat transfer in stenosis narrow arteries, *J. Magn. Magn. Mater.* 569 (2023) 170448.
- [24] Z. Abbas, M.Y. Rafiq, J. Hasnain, A. Nadeem, Thermally developed generalized Bödewadt flow containing nanoparticles over a rotating surface with slip condition, *Int. Commun. Heat Mass Transfer* 122 (2021) 105143.
- [25] A.S. Alnahdi, S. Nasir, T. Gul, Couple stress ternary hybrid nanofluid flow in a contraction channel by means of drug delivery function, *Math. Comput. Simul.* 210 (2023) 103–119.
- [26] R. Gandhi, B.K. Sharma, Q.M. Al-Mdallal, H.V.R. Mittal, Entropy generation and shape effects analysis of hybrid nanoparticles (Cu-Al₂O₃/blood) mediated blood flow through a time-variant multi-stenotic artery, *International Journal of Thermofluids* 18 (2023) 100336.
- [27] N. Hameed, S. Noeiaghdam, W. Khan, B. Pimpunchat, U. Fernandez-Gamiz, M.S. Khan, A. Rehman, Analytical analysis of the magnetic field, heat generation and absorption, viscous dissipation on couple stress casson hybrid nano fluid over a nonlinear stretching surface, *Results in Engineering* 16 (2022) 100601.
- [28] M.Y. Rafiq, Z. Abbas, Impacts of viscous dissipation and thermal radiation on Rabinowitsch fluid model obeying

- peristaltic mechanism with wall properties, *Arab. J. Sci. Eng.* 46 (2021) 12155–12163.
- [29] U. Khanduri, B.K. Sharma, in: *Mathematical analysis of Hall Effect and Hematocrit Dependent Viscosity on au/GO-Blood Hybrid Nanofluid Flow Through a Stenosed Catheterized Artery With Thrombosis*, Springer Nature Switzerland, Cham, 2023, pp. 121–137.
- [30] R. Gandhi, B.K. Sharma, in: *Modelling Pulsatile Blood Flow Using Casson Fluid Model Through an Overlapping Stenotic Artery With Au-Cu Hybrid Nanoparticles: Varying Viscosity Approach*, Springer Nature Switzerland, Cham, 2023, pp. 155–176.
- [31] J.V. Tawade, C.N. Guled, S. Noeiaghdam, U. Fernandez-Gamiz, V. Govindan, S. Balamuralitharan, Effects of thermophoresis and Brownian motion for thermal and chemically reacting Casson nanofluid flow over a linearly stretching sheet, *Results in Engineering* 15 (2022) 100448.
- [32] R. Gupta, M. Gaur, Q. Al-Mdallal, S.D. Purohit, D.L. Suthar, Numerical study of the flow of two radiative nanofluids with Marangoni convection embedded in porous medium, *J. Nanomater.* 2022 (2022) 1–7.
- [33] K.S. Nisar, U. Khan, A. Zaib, I. Khan, A. Morsy, A novel study of radiative flow involving micropolar nanofluid from a shrinking/stretching curved surface including blood gold nanoparticles, *The European Physical Journal Plus* 135 (10) (2020) 1–19.
- [34] M.I. Khan, S. Ullah, T. Hayat, M. Waqas, M.I. Khan, A. Alsaedi, Salient aspects of entropy generation optimization in mixed convection nanomaterial flow, *Int. J. Heat Mass Transf.* 126 (2018) 1337–1346.
- [35] M. Sharma, B.K. Sharma, U. Khanduri, N.K. Mishra, S. Noeiaghdam, U. Fernandez-Gamiz, Optimization of heat transfer nanofluid blood flow through a stenosed artery in the presence of Hall effect and hematocrit dependent viscosity. *Case Studies, Therm. Eng.* 103075 (2023).
- [36] S. Arulmozhi, K. Sukkiramathi, S.S. Santra, R. Edwan, U. Fernandez-Gamiz, S. Noeiaghdam, Heat and mass transfer analysis of radiative and chemical reactive effects on MHD nanofluid over an infinite moving vertical plate, *Results in Engineering* 14 (2022) 100394.
- [37] M.I. Khan, M. Waqas, T. Hayat, M.I. Khan, A. Alsaedi, Chemically reactive flow of upper-convected Maxwell fluid with Cattaneo-Christov heat flux model, *J. Braz. Soc. Mech. Sci. Eng.* 39 (2017) 4571–4578.
- [38] F. Ali, M. Awais, A. Ali, N. Vrinceanu, Z. Shah, V. Tirth, Intelligent computing with Levenberg–Marquardt artificial neural network for Carbon nanotubes-water between stretchable rotating disks, *Sci. Rep.* 13 (1) (2023) 3901.
- [39] I. Khan, M.A.Z. Raja, M.A.R. Khan, M. Shoaib, S. Islam, Z. Shah, Design of backpropagated intelligent networks for nonlinear second-order Lane-Emden pantograph delay differential systems, *Arab. J. Sci. Eng.* 47 (2) (2022) 1197–1210.
- [40] I. Khan, M.A.Z. Raja, M. Shoaib, P. Kumam, H. Alrabaiah, Z. Shah, S. Islam, Design of neural network with Levenberg-Marquardt and Bayesian regularization backpropagation for solving pantograph delay differential equations, *IEEE Access* 8 (2020) 137918–137933.
- [41] K. Ahmed, T. Akbar, T. Muhammad, Physical aspects of homogeneous-heterogeneous reactions on MHD Williamson fluid flow across a nonlinear stretching curved surface together with convective boundary conditions, *Math. Probl. Eng.* 2021 (2021) 1–13.
- [42] M. Sajid, N. Ali, T. Javed, Z. Abbas, Stretching a curved surface in a viscous fluid, *Chin. Phys. Lett.* 27 (2) (2010) 024703.
- [43] P.K. Dadheech, P. Agrawal, A. Sharma, K.S. Nisar, S.D. Purohit, Marangoni convection flow of γ -Al₂O₃ nanofluids past a porous stretching surface with thermal radiation effect in the presence of an inclined magnetic field, *Heat Transfer* 51 (1) (2022) 534–550.
- [44] M.I. Khan, F. Alzahrani, Optimized framework for slip flow of viscous fluid towards a curved surface with viscous dissipation and Joule heating features, *Appl. Math Comput.* 417 (2022) 126777.
- [45] M.I. Khan, T.A. Khan, S. Qayyum, T. Hayat, M.I. Khan, A. Alsaedi, Entropy generation optimization and activation energy in nonlinear mixed convection flow of a tangent hyperbolic nanofluid, *The European Physical Journal Plus* 133 (2018) 1–20.
- [46] A.S. Alnahdi, S. Nasir, T. Gul, Blood-based ternary hybrid nanofluid flow-through perforated capillary for the applications of drug delivery, *Waves Random Complex Media* (2022) 1–19.
- [47] B.K. Sharma, U. Khanduri, N.K. Mishra, K.S. Mekheimer, Combined effect of thermophoresis and Brownian motion on MHD mixed convective flow over an inclined stretching surface with radiation and chemical reaction, *Int. J. Mod Phys B* 2350095 (2022).
- [48] A. Tassaddiq, S. Khan, M. Bilal, T. Gul, S. Mukhtar, Z. Shah, E. Bonyah, Heat and mass transfer together with hybrid nanofluid flow over a rotating disk, *AIP Adv.* 10 (5) (2020) 055317.
- [49] W. Al-Kouz, K. Swain, B. Mahanthesh, W. Jamshed, Significance of exponential space-based heat source and inclined magnetic field on heat transfer of hybrid nanofluid with homogeneous-heterogeneous chemical reactions, *Heat Transfer* 50 (4) (2021) 4086–4102.
- [50] S.M. Upadhyaya, S.S.R. Raju, C.S.K. Raju, N.A. Shah, J.D. Chung, Importance of entropy generation on Casson, Micropolar and Hybrid magneto-nanofluids in a suspension of cross diffusion, *Chin. J. Phys.* 77 (2022) 1080–1101.
- [51] M.N. Khan, N.A. Ahammad, S. Ahmad, M.A. Elkotb, E. Tageldin, K. Guedri, M.F. Yassen, Thermophysical features of Ellis hybrid nanofluid flow with surface-catalyzed reaction and irreversibility analysis subjected to porous cylindrical surface. *Frontiers, Physics* 795 (2022).
- [52] B.K. Sharma, C. Kumawat, O.D. Makinde, Hemodynamical analysis of MHD two phase blood flow through a curved permeable artery having variable viscosity with heat and mass transfer, *Biomech. Model. Mechanobiol.* 21 (3) (2022) 797–825.
- [53] B.K. Sharma, Poonam, & Chamkha, A. J., Effects of heat transfer, body acceleration and hybrid nanoparticles (Au–Al₂O₃) on MHD blood flow through a curved artery with stenosis and aneurysm using hematocrit-dependent viscosity, *Waves Random Complex Media* 1–31 (2022), <https://doi.org/10.1080/17455030.2022.2125597>.
- [54] B.K. Sharma, A. Kumar, R. Gandhi, M.M. Bhatti, N.K. Mishra, Entropy Generation and Thermal Radiation Analysis of EMHD Jeffrey Nanofluid Flow: Applications in Solar Energy, *Nanomaterials* 13 (3) (2023) 544.
- [55] R. Gandhi, B.K. Sharma, C. Kumawat, O.A. Bég, Modeling and analysis of magnetic hybrid nanoparticle (Au–Al₂O₃/blood) based drug delivery through a bell-shaped occluded artery with joule heating, viscous dissipation and variable viscosity effects, Part E: *Journal of Process Mechanical Engineering* 236 (5) (2022) 2024–2043.